JGR Solid Earth

RESEARCH ARTICLE
10.1029/2022JB024918

Seismicity, Fault Architecture, and Slip Mode of the Westernmost Gofar Transform Fault

Jianhua Gong[1] and **Wenyuan Fan**[1]

[1]Scripps Institution of Oceanography, UC San Diego, La Jolla, CA, USA

Key Points:

- The westernmost Gofar transform fault is composed of distinct seismic and aseismic zones
- These fault zones are controlled by different slip modes and they possibly interact with each other via multiple mechanisms
- The slip mode variations may result from the complex fault architecture and fluid–rock interactions at multiple scales

Supporting Information:

Supporting Information may be found in the online version of this article.

Correspondence to:

J. Gong,
j4gong@ucsd.edu

Citation:

Gong, J., & Fan, W. (2022). Seismicity, fault architecture, and slip mode of the westernmost Gofar transform fault. *Journal of Geophysical Research: Solid Earth*, *127*, e2022JB024918. https://doi.org/10.1029/2022JB024918

Received 5 JUN 2022
Accepted 23 OCT 2022

Author Contributions:

Conceptualization: Jianhua Gong, Wenyuan Fan
Formal analysis: Jianhua Gong, Wenyuan Fan
Funding acquisition: Wenyuan Fan
Investigation: Jianhua Gong, Wenyuan Fan
Methodology: Jianhua Gong, Wenyuan Fan
Supervision: Wenyuan Fan
Writing – original draft: Jianhua Gong, Wenyuan Fan
Writing – review & editing: Jianhua Gong, Wenyuan Fan

Abstract Oceanic transform faults accommodate plate motions through both seismic and aseismic slips. However, deformation partition and slip mode interaction at these faults remain elusive mainly limited by rare observations. We use 1-year ocean bottom seismometer data collected in 2008 to detect and locate earthquakes at the westernmost Gofar transform fault. The ultra-fast slipping rate of Gofar results in ∼30,000 earthquakes during the observational period, providing an excellent opportunity to investigate interrelations between the slip mode, seismicity, and fault architecture at an unprecedented resolution. Earthquake distribution indicates that the ∼100-km-long Gofar transform fault is distinctly segmented into five zones, including one zone contouring a M6 earthquake that was captured by the experiment. Further, a barrier zone east of the M6 earthquake hosted abundant foreshocks preceding the M6 event and halted its active seismicity afterward. The barrier zone has two layers of earthquakes at depth, and they responded to the M6 earthquake differently. Additionally, a zone connecting to the East Pacific Rise had quasi-periodic earthquake swarms. The seismicity segmentation suggests that the Gofar fault has multiple slip modes occurring in adjacent fault patches. Spatiotemporal characteristics of the earthquakes suggest that complex fault architecture and fluid–rock interaction play primary roles in modulating the slip modes at Gofar, possibly involving multiple concurrent physical processes.

Plain Language Summary Oceanic transform faults are apparently simple tectonic plate boundaries. However, their structures are surprisingly complex as manifested through various seismic and aseismic slip modes. The deformation partition mechanism is not well understood due to a lack of near-field observations. Here, we use 1-year ocean bottom seismometer data to study earthquakes at the westernmost Gofar transform fault and use these earthquakes to infer the fault slip modes. Spatiotemporal evolution of the earthquakes suggests that the fault has five distinctive zones along strike, including one zone hosted a magnitude (M) 6 earthquake captured by the experiment. The remaining zones are dominated by either seismic or aseismic slip. Such distinct variations of slip mode along strike likely originated from the complex, heterogeneous fault structure, and extensive fluid–rock interactions.

1. Introduction

Both seismic and aseismic slip can consume the total slip budget to accommodate plate motions (Avouac, 2015; Harris, 2017; Wolfson-Schwehr & Boettcher, 2019). The two slip modes dominate different fault patches and show variations along both the strike and dip directions (e.g., Han et al., 2017; Y. Liu & Rice, 2005; Y. K. Liu et al., 2022; Scholz, 1998). For example, earthquakes and slow earthquakes occur at subduction zone with different types of events dominating megathrust segments at varying depths (Lay et al., 2012; Obara & Kato, 2016; Wirth et al., 2022). Oceanic transform faults (OTFs) also slip in both modes with 15%–35% of the slip budget released through earthquakes and the rest as aseismic slips (Boettcher & Jordan, 2004; Y. Liu et al., 2012; Wolfson-Schwehr & Boettcher, 2019). The two slip modes at OTFs switch intermittently with variations predominately along the strike direction (McGuire et al., 2012; Shi et al., 2021). Moderate to large magnitude OTF earthquakes often repeatedly occur on isolate segments that are likely surrounded by creeping segments (e.g., Castellanos et al., 2020; Shi et al., 2021). For example, $M \geq 6$ earthquakes quasi-periodically rupturing the same fault patches have been observed at multiple OTF systems, including Gofar (McGuire, 2008), Discovery (Wolfson-Schwehr et al., 2014), Blanco (Braunmiller & Nábělek, 2008), Eltanin (Sykes & Ekström, 2012), and Charlie–Gibbs (Aderhold & Abercrombie, 2016). Such regular earthquake-cycle behaviors are rarely observed in other fault systems (Bakun et al., 2005). Further, these regular $M \geq 6$ earthquakes are frequently preceded with abundant foreshocks (Aderhold & Abercrombie, 2016; McGuire et al., 2005, 2012). These systematic patterns of OTF earthquakes suggest that their regulating physical processes are repeatable and the processes seem to be

controlled by their slip modes and fault architecture. Therefore, understanding the slip modes as well as the fault architecture is critical in illuminating the underlining earthquake physics.

Fault architecture and slip mode partition are imprinted in microearthquakes (Y. K. Liu et al., 2022; Vidale et al., 1994). Particularly, interaction and triggering among different fault segments are often manifested as transient earthquake sequences lasting from seconds to years (Freed, 2005). For example, earthquakes can trigger afterslip to generate aftershocks (Hsu et al., 2006; Jiang et al., 2021), and accelerating aseismic slips are often accompanied by migrating earthquakes, which may eventually initiate large earthquakes (Kato et al., 2012; McLaskey, 2019; Shelly, 2009). Additionally, stress transfer and fluid migration can influence earthquakes at different fault segments over a large spatial footprint (e.g., Ross et al., 2020). Hence, investigating microearthquakes can help deciphering fault segmentation, slip partition, fault architecture, and mechanical controls of earthquake rupture dynamics (e.g., Hardebeck et al., 1998; Y. K. Liu et al., 2022; Trugman et al., 2016).

Despite OTFs exhibit some of the most predictable and systematic earthquake behaviors, details of their fault architecture and slip partition mechanisms are not well understood, mainly limited by rare near-field observations (e.g., Parnell-Turner et al., 2022). However, remarkable details of the fault structures can be learned from microearthquakes when ocean bottom seismometer (OBS) data are available (Gong et al., 2022; Hicks et al., 2020; Kuna et al., 2019; McGuire et al., 2012; Wolfson-Schwehr et al., 2014; Yu et al., 2021). For example, barrier zones that separate repeating rupture patches are observed at Blanco and Gofar transform systems (Kuna et al., 2019; McGuire et al., 2012). Deep seismicity at 10–30 km are found from fast to slow slipping OTFs (Gong et al., 2022; Kuna et al., 2019; Yu et al., 2021), providing new insights into elastic failure conditions (Kohli et al., 2021; Prigent et al., 2020).

Previous studies usually report a few thousand earthquakes for an 1-year OBS experiment (e.g., Hicks et al., 2020; Kuna et al., 2019). The catalog size may reflect challenges in picking emergent *P* waves and is also likely due to the coarse OBS array configurations (Hicks et al., 2020; Kuna et al., 2019; McGuire et al., 2012). Recent applications of machine-learning phase pickers to OBS data have produced multiple times more robust *P* and *S* phase picks than those from conventional approaches (Allen, 1978; Maeda, 1985; Ruppert et al., 2021; Saragiotis et al., 2002). For example, the advancement enables locating ∼24,000 earthquakes with a magnitude of completeness around 0.8 at the Quebrada transform fault system, revealing deep seismicity clouds that are likely controlled by aseismic slip and fluid circulation (e.g., Gong et al., 2022).

Here, we investigate earthquakes at the westernmost segment of the Gofar transform system (G3) using 1-year OBS data collected in 2008 (McGuire et al., 2012). The deployment captured an anticipated M6 earthquake at G3 and recorded the late and early stages of an M6 earthquake seismic cycle. The experiment offers a unique opportunity to investigate the fault architecture, seismicity evolution, and their interrelations in regulating earthquake rupture processes. Particularly, the active seismicity in the region provides a great opportunity to distinguish fault segmentation and the associated slip modes.

We apply a suite of techniques to detect, locate, and relocate earthquakes at G3 using the OBS data. Spatiotemporal evolution of the earthquakes suggests that the ∼100-km-long Gofar fault has complex internal structures and is segmented into five zones with their seismicity dominantly but not exclusively influenced by one of the two slip modes. Further, deep seismicity is a common feature of the eastern G3 but absent at the western end, suggesting different temperatures and seismogenic depths along strike. Moreover, fault segments slipping aseismically have abundant microearthquakes. These segments are likely heavily damaged with heterogeneously distributed asperities, and their seismicity evolution implies intense fluid–rock interactions.

2. Gofar Transform Fault System

The Gofar transform fault system is located ∼4.4°S at the East Pacific Rise (EPR, Figure 1). It consists of three segments denoted as G1–G3 from east to west that are connected by two short intratransform spreading centers (ITSCs; Pickle et al., 2009). Gofar transform fault system is at an ultra-fast spreading center that slips at a rate of ∼140 mm/year (Wolfson-Schwehr & Boettcher, 2019). The Gofar faults have magnitude 5–6 earthquakes quasi-periodically at the same locations with a recurrence period of 5–6 years (McGuire, 2008; Wolfson-Schwehr et al., 2014).

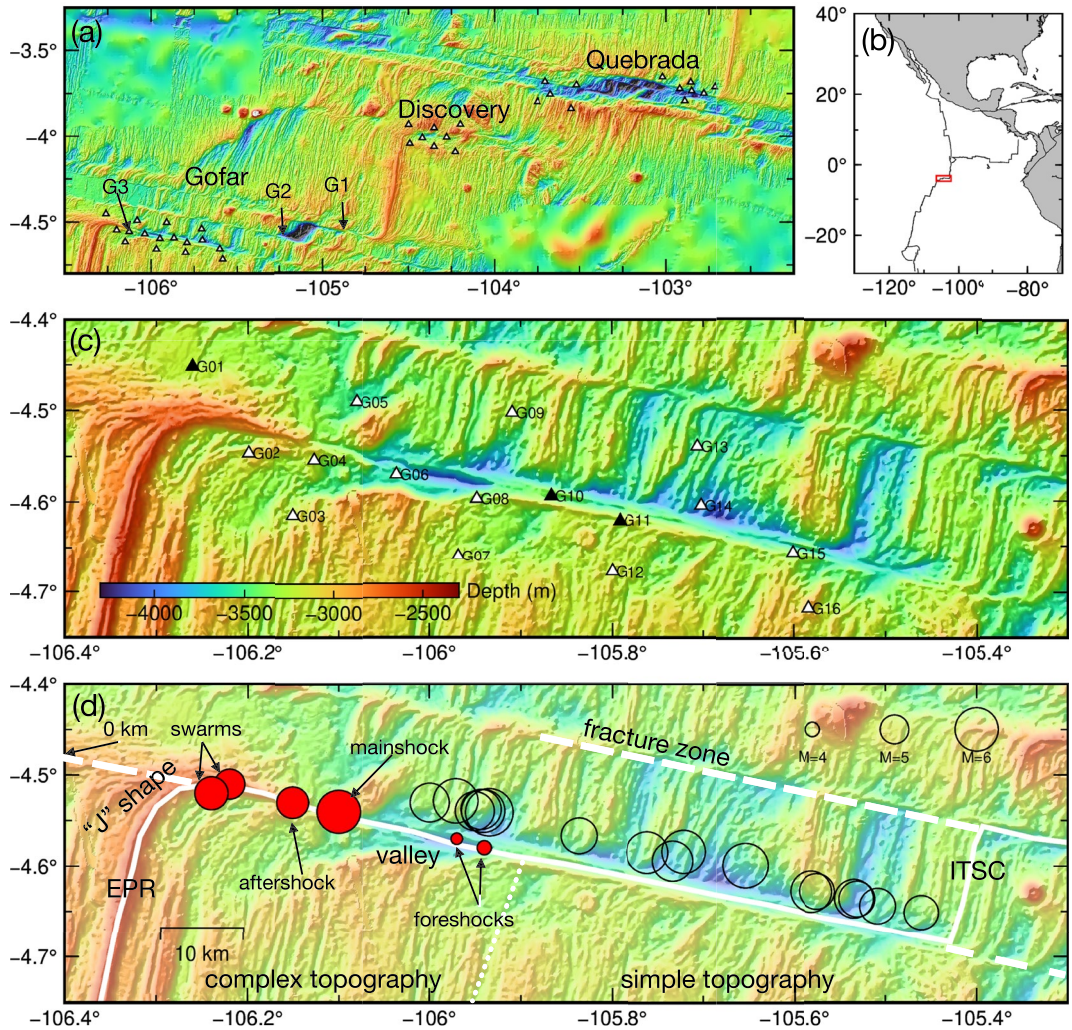

Figure 1. Bathymetry and structural interpretation of the westernmost Gofar transform fault. (a) Bathymetry of the Quebrada–Discovery–Gofar (QDG) transform system. White triangles are OBS stations of the 2008 QDG experiment. Three segments of the Gofar transform system, G1–G3, are labeled on the map from east to west. (b) Zoom-out map showing the location of the QDG system (red rectangular). (c) Bathymetry of the study area. White triangles are functioning OBS stations in this study and black triangles are malfunctioned stations. (d) Structural interpretation of study area. Solid white lines mark the trace of ridges and transform faults. White dash lines denote fracture zones. "J"-shape structure and deep valley are denoted on the map. Red solid circles are the epicenters of the 2008 M6 mainshock, its largest aftershock, two M5 events during December swarm, and three M4 events in the barrier zone (two overlaps). Black open circles are $M \geq 5$ earthquake locations from Shi et al. (2021). Intersection between the fracture zone and the west boundary of the map marks the origin (0 km) of the along-strike distance. Dot line indicates a separation of complex topography on the seafloor in the west part of G3 and simple topography in the east part of G3. EPR stands for East Pacific Rise. ITSC stands for intratransform spreading center.

The G3 fault branch shows clear along-strike variations in the surface topography (Figure 1). The western part of the fault connects to EPR, showing a "J"-shape structure with high elevation (Grevemeyer et al., 2021). Adjacent to the "J"-structure, there is a ∼10-km-long deep valley developed along the strike direction at ∼106°W with a maximum depth of ∼4,100 m. The valley is bounded by high-elevation flanks on both the north and south sides of G3. The eastern topography of G3 is relatively simple with a linear shallow valley coinciding with the fault. The G3 fault connects a short ITSC at the east end, which has a lower elevation and a narrower width compared to EPR, indicating limited magma supply beneath the ITSC (Pickle et al., 2009).

Using the 2008 OBS data, McGuire et al. (2012) identified that G3 has fault patches with distinct seismicity characteristics. East of the M6 fault patch, there is a barrier zone that had intense seismicity from shallow to

deep but halted the activity after the M6 mainshock. West of the M6 fault patch, a 2-week-long intense swarm occurred in December 2008 at a fault segment adjacent to EPR. The seismicity variation suggests the G3 fault patches slipping in different modes. Traveltime tomographic models show low Vp/Vs ratios in the barrier zone and high Vp/Vs ratios in the M6 rupture area, suggesting that the two patches have different fault-zone materials (Froment et al., 2014; Guo et al., 2018). Long-term records reveal that $M \sim 6$ earthquakes rupture two sections of the G3 fault quasi-periodically (Shi et al., 2021). The western section is at the 2008 M6 earthquake zone and the other section is eastern of the barrier zone. The barrier zone is absent of $M \geq 5$ earthquakes, likely controlled by the aseismic slip mode (Shi et al., 2021; Wolfson-Schwehr et al., 2014).

3. Data and Methods

3.1. Data

The 2008 Quebrada–Discovery–Gofar marine seismic experiment deployed 30 broadband and 10 short-period three-component OBSs across the three fault systems with 16 broadband OBSs on the G3 segment, aiming to capture an anticipated M6 event (Figure 1). Seven of the 16 OBS stations also had collocated strong motion sensors. The stations were situated in water depths ranging from 2,960 to 3,930 m. The OBSs recorded waveform data at a sampling rate of either 50 or 100 Hz (see Table S1 in Supporting Information S1 for details). Stations G01, G11, and G15 did not record useful data and we do not analyze their waveforms. During the experiment, an M6 event occurred on 18 September 2008 and triggered an M5 aftershock in the western section of the fault patch ∼20 min after the mainshock (Figure 1). Another two M5 events occurred near the ridge–transform intersection in December 2008 as part of an energetic earthquake sequence.

3.2. Earthquake Detection, Location, and Magnitude Calculation

We follow Gong et al. (2022) to apply a four-step workflow to detect, associate, locate, and relocate earthquakes using open-source software (see Data Availability Statement). We first apply a machine-learning phase picker, EQTransformer, to detect *P* and *S* wave arrivals (Mousavi et al., 2020). EQTransformer is a deep-learning model that can simultaneously detect earthquakes and pick phase arrivals with uncertainty quantification. In our case, the waveforms of Gofar earthquakes have short *S*–*P* times than those used in the EQTransformer training data set (Mousavi et al., 2019). Therefore, we upsample the data by a factor of 1 (no upsampling), 2, or 4 before applying EQTransformer (e.g., Gong et al., 2022; R. Wang et al., 2020). The upsampling factor is station-dependent and is determined through trial-and-error exercises by experimenting the factors on 1-month-long data at each station. The optimal upsampling factor is selected as the one yielding most phase picks (see Table S1 in Supporting Information S1 for details). In total, we detect ∼515,000 *P* arrivals and ∼524,000 *S* arrivals.

The phase picks are then associated using REAL (Zhang et al., 2019). REAL grid searches for a candidate location and time to associate the phase picks by counting the number of *P* and *S* picks and computing the traveltime residuals. We require a successful association to have at least three *P* picks and one *S* picks and a residual arrival time tolerance of 0.5 s. The association uses a one-dimensional (1D) *P* wave velocity profile (Figure S1 in Supporting Information S1) extracted from a two-dimensional (2D) *P* wave traveltime tomographic model of the Gofar system (Roland et al., 2012). A 1D *S* wave velocity model is then converted from the 1D *P* wave model by assuming a constant Vp/Vs ratio of 1.9 in the crust (above 6.85 km depth) and 1.8 in the mantle (below 6.85 km depth). Regions within 0.2° radius of the station that records the earliest phase arrival are searched with a depth extent up to 20 km. The searching regions are gridded at 0.01° horizontally and 0.5 km vertically. In total, we identify 47,220 candidate earthquakes from the association step.

We use COMPLOC to determine the earthquake absolute locations using the associated *P* and *S* wave arrival times (G. Lin & Shearer, 2006). The COMPLOC algorithm corrects a source-specific station term when solving for local earthquake locations, which can improve the location accuracy by empirically removing the systematic effects of three-dimensional velocity structures (G. Lin & Shearer, 2005; Richards-Dinger & Shearer, 2000). Additionally, we use ℓ_1 norm to evaluate the traveltime residuals which is insensitive to phase-pick outliers. Some earthquake locations cannot be resolved due to the station configuration, and they are erroneously placed at the seafloor (e.g., Gong et al., 2022). We have visually inspected waveforms of such earthquakes and conclude that these shallow earthquakes are likely mislocated. Therefore, we remove events within 1 km depth to the seafloor,

apply the COMPLOC method to locate remaining events, and iterate this procedure 40 times till the final results are stable (Figure S2 in Supporting Information S1). The procedure results 30,855 locatable events (Figure 2).

The earthquake locations are further refined using waveform cross-correlation data. We apply the GrowClust relocation method to the differential times obtained from cross-correlating *P* and *S* waveforms of adjacent event pairs to achieve high-precision relative earthquake locations (Trugman & Shearer, 2017). We cross-correlate body waveforms of the closest 100 events with those of each earthquake to obtain the differential traveltimes. We successfully relocate 30,854 earthquakes in total (Figure 2). This final location catalog is referred to as the GrowClust catalog.

For the relocated earthquakes, local magnitudes (M_L) are calculated using three-component displacement waveforms. We first remove the instrument response and convolve the records with the Wood-Anderson instrument response. The waveforms are then filtered between 4 and 20 Hz and windowed from 1 s before to 5 s after the *S* arrivals. A peak amplitude (A) is calculated as the maximum root sum square of the windowed three-component displacements. We also measure the peak noise amplitude (A_N) using the same approach but apply to a window of 5–2 s before the *P* arrivals. The local magnitude is computed as

$$M_L = \log_{10} A + 2.56\log_{10} D - 1.67, \quad (1)$$

where D is the hypocentral distance. We only keep a local magnitude estimate at a given station if the signal-to-noise ratio (A/A_N) is greater than 10. The final M_L of the earthquake is estimated as the median value of M_L computed for all the available stations, and we discard the magnitude estimate if less than five stations had qualified measurements. We eventually obtain M_L for 6,164 earthquakes, which populates a catalog named as the automated catalog. The magnitude–frequency distribution of these earthquakes is shown in Figure S3a in Supporting Information S1. The magnitudes are unusually small. It is likely that the coefficients in Equation 1 are different for Gofar as they were derived for Southern California. Therefore, we calibrate our local magnitude estimates by using the moment magnitudes of 115 earthquakes that were derived from displacement spectrum (Moyer et al., 2018). We apply a constant shift of 0.65 to our local magnitude estimates (see Text S1 and Figure S3b in Supporting Information S1). The final catalog has a magnitude completeness of 0.6 and a *b*-value of 0.75 obtained from the maximum curvature method and maximum likelihood method respectively (Figure S3d in Supporting Information S1; Aki, 1965; Wiemer & Wyss, 2000).

3.3. Earthquake Clustering

In addition to solving for relative locations, GrowClust applies a hierarchical clustering algorithm that cluster events based on waveform cross-correlation coefficients (Trugman & Shearer, 2017). The algorithm first defines a similarity coefficient that serves as a metric to measure waveform similarity between event pairs and then forms earthquake clusters based on the similarity coefficients (Trugman & Shearer, 2017). A cluster represents a set of events that are spatially close and have similar waveforms, which indicate that they might come from the same fault patch and share similar focal mechanisms. The number of clusters for a given catalog is influenced by the GrowClust parameters. We have experimented with seven sets of input parameters, and the results of each set are described in Text S2 in Supporting Information S1. We opt to a set of parameters that generates few off-fault clusters and are free from unrealistic gaps between seismicity strands (Figures S4 and S5 in Supporting Information S1). The set of parameters leads to 34 clusters, and each cluster has more than 100 events (Figure S6 in Supporting Information S1). These clusters include 84% of the total seismicity (Table S2 in Supporting Information S1). We focus on these 34 clusters in the following analysis. We further inspect the temporal behaviors of the clusters that are adjacent to each other and merge clusters if they show similar evolution in seismicity rate (Figure S7 in Supporting Information S1).

3.4. Locating Missing Earthquakes

Visual inspection of daily waveforms suggests that there are missing events in the GrowClust catalog, which have clear, large amplitudes. For example, the M6 mainshock and the M5 aftershock are missing from the catalog (Figure S8 in Supporting Information S1). We speculate that these events are missed because the training data sets of EQTransformer have limited near-field waveforms of $M \geq 5$ events (Mousavi et al., 2019). Further, Gofar earthquakes tend to generate emergent arrivals on OBS, posing challenges in detecting body waves using such

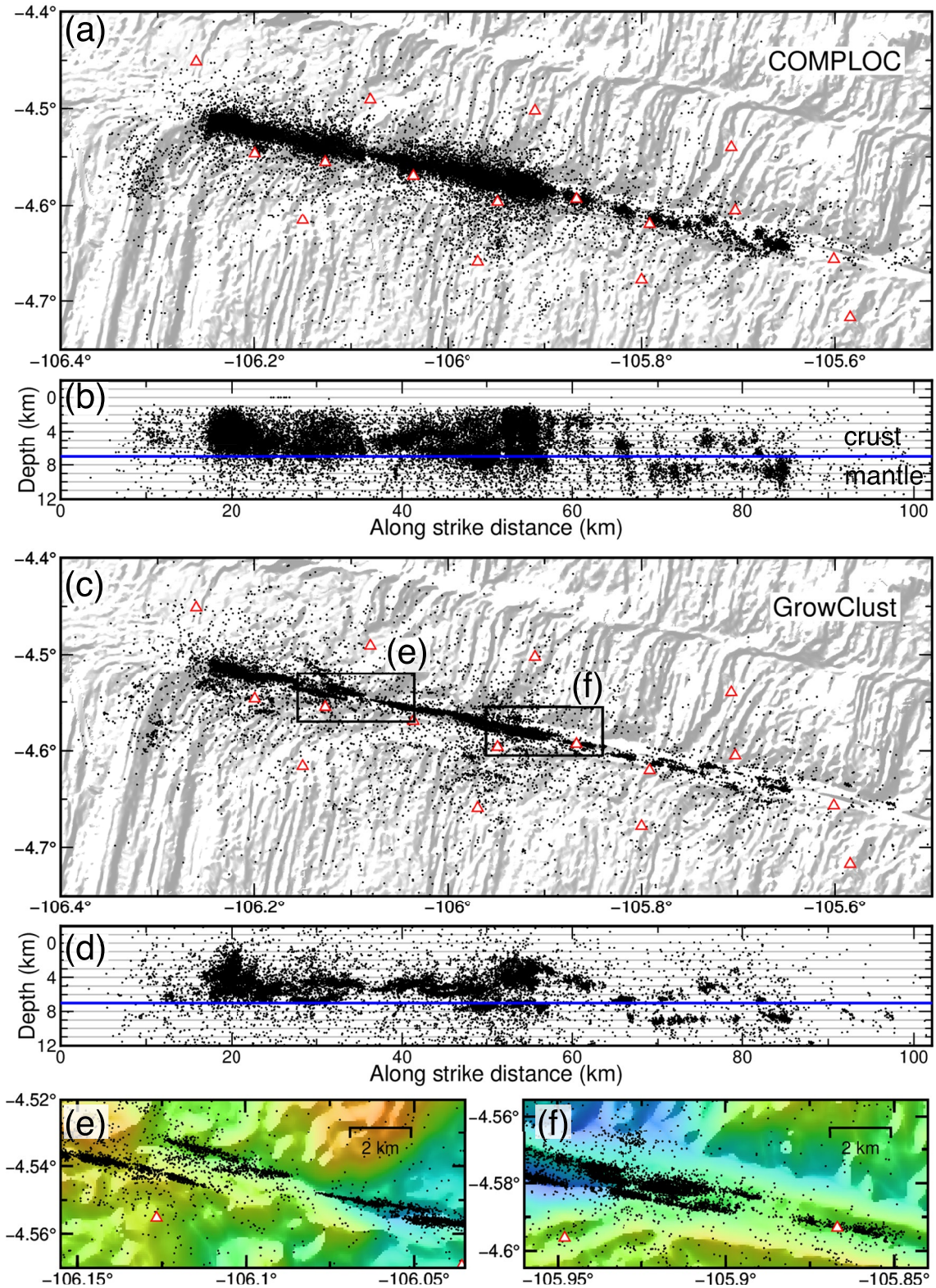

Figure 2. Earthquake location and relocation results. (a, b) Map and depth views of the COMPLOC earthquake locations. (c, d) Map and depth views of the GrowClust earthquake relocations. Blue lines mark the 7 km depth, which we infer as the local Moho discontinuity. (e, f) Zoom-in views of two rectangular areas in (c). Background color denotes seafloor bathymetry using the same color scale as in Figure 1. White open triangles are OBS stations.

phase pickers. Finally, the iterative location procedure also removes 35% events in the COMPLOC location step (Figure S2 in Supporting Information S1).

In recognizing these challenges, we examine continuous waveforms to search for missing events whose amplitudes exceed a threshold of $\sim 1.2 \times 10^{-4}$ m/s (74,866 unit count) at more than one station (see Text S1 in Supporting Information S1 for details). Specifically, 397 events are manually identified through this approach including the M6 mainshock, its largest aftershock, and two M5 events during the December swarm (Figure S8 in Supporting Information S1). We hand pick their P and S arrivals when possible and then locate these events using a grid-search procedure. We search a region from −4.75° to −4.4° in latitude and from −106.4° to −105.5° in longitude, with a grid spacing of 0.01° in both horizontal directions, respectively. The event depth is searched from 0 to 15 km, with an intergrid spacing of 0.5 km. The misfit ($E(i)$) at the ith searching grid is defined as

$$E(i) = \frac{1}{N} \sum_{j=1}^{N} \left| \overline{T}_X^{pre}(i,j) - \overline{T}_X(j) \right|, \tag{2}$$

where $\overline{T}_X^{pre}(i,j)$ is the demeaned predicted P or S wave traveltime from grid-i to station-j, and $\overline{T}_X(j)$ is the demeaned observed P or S wave arrival time at station-j, and N is the number of available stations. The demeaned traveltimes are defined as

$$\overline{T}_X^{pre}(i,j) = T_X^{pre}(i,j) - \frac{1}{N} \sum_{k=1}^{N} T_X^{pre}(i,k) \tag{3}$$

and

$$\overline{T}_X(j) = t_X(j) - \frac{1}{N} \sum_{k=1}^{N} t_X(k), \tag{4}$$

where $T_X^{pre}(i,j)$ and $t_X(j)$ are the predicted and observed P or S wave traveltimes from grid-i to station-j, respectively. The predicted P or S wave traveltime is calculated using the same velocity model as being used for determining the COMPLOC locations. The best location estimate yields the minimum misfit. We consider the event depth cannot be constrained when the depth is placed shallower than 1 km or deeper than 12 km. In such cases, the event depth is assigned as 5 km. The final locations of these events are shown in Figure S9 in Supporting Information S1. We do not relocate these events because their waveforms are dissimilar to those of nearby small magnitude earthquakes. Earthquake magnitudes of these earthquakes are calculated in the same way as for earthquakes in the automated catalog.

Some strong events are included in the GrowClust catalog but without local magnitude estimates because of having less than five qualified S picks. To identify these earthquakes, we further scan the waveforms of events in the GrowClust catalog using the same technique and threshold as above (74,866 unit count). Once an event is identified as a potential strong event, we use predicted S arrival times instead of EQTransformer S picks to window the waveforms for amplitude measurements. The local magnitude is calculated using the same procedure and criteria as for the automated catalog. In total, 299 additional events in the automated catalog obtained local magnitude estimates. Hereinafter, we refer to the two sets of events from scanning the waveforms as the manual catalog. The combination of the automated and manual catalogs leads to a combined catalog.

3.5. Coulomb Stress Change

To understand interrelations of the earthquake sequences, we compute Coulomb stress changes due to the M6 mainshock imposed on other G3 fault patches (King et al., 1994; J. Lin & Stein, 2004; Stein et al., 1997; J. Wang et al., 2021). No finite-fault model is available for this earthquake. For simplicity, we assume a uniform slip model rupturing a rectangular fault patch based on $M_0 = \mu DA$, where M_0 is the seismic moment, μ is the shear modules, A is the rupture area, and D is the average slip. We consider a range of possible slip areas and the details are discussed in Section 5.1.1. The fault geometry, including the strike, dip, and rake, of both the source fault and the receiver fault is 102°, 90°, and 0°. We also assume the earthquake with a moment magnitude of 6.0 (Bondár & Storchak, 2011; Ekström et al., 2012) and the fault with a shear modules of 40 GPa. Results of Coulomb

stress changes at various depths are shown in Figure S10 in Supporting Information S1. The stress changes are computed assuming a frictional coefficient of 0.4.

4. Results

Seismicity at G3 shows strong spatial and temporal variations in both the along-strike and along-dip (depth) directions (Figures 2 and 3). In general, the seismicity trends agree well with the seafloor fault traces (Figure 2). Majority of earthquakes (60%) are located in between 4 and 7 km in depth (Figure 2). We consider that earthquakes shallower than 7 km are crustal events and the deeper ones are upper-mantle earthquakes, following the 1D velocity model used for earthquake location (Figure S1 in Supporting Information S1). Two prominent seismicity sequences occurred during the deployment, namely, the foreshock–mainshock–aftershock sequence of the 18 September M6 earthquake and the 6–20 December swarm sequence (Figure 3).

We manually inspect and group the 34 clusters into five zones that are named Zone 1 to Zone 5 from east to west (Figure S7 and Table S2 in Supporting Information S1). The earthquakes are grouped into the same zones if they are spatially connected and have similar temporal evolution. Particularly, the cluster responses to the M6 mainshock and the December swarm are diagnostic in associating the clusters (Figure S7 in Supporting Information S1). The 34 clusters are sorted by their centroid longitude, and they are indexed as clusters 0–33 from west to east. The easternmost six clusters (clusters 28–33) are around the eastern M6 fault patch, and they did not obviously respond to the two sequences. Therefore, these clusters are grouped into Zone 1. West of Zone 1, clusters 20–23, 25, and 27 had energetic foreshocks but were absent of aftershocks after the M6 earthquake, and they are grouped into Zone 2. Clusters 24 and 26 are considered as part of Zone 2 because of their similar along-strike locations, even though their seismicity rates did not decrease abruptly after the M6 earthquake. Seismicity rates of clusters 15 and 17–19 increased abruptly after the M6 earthquake, likely contouring the mainshock slip area, and therefore are combined into Zone 3. Cluster 16 is also part of Zone 3 as it is located right beneath clusters 15 and 17. Clusters 11–14 are combined into Zone 4 since their seismicity rates seem to be modulated by both the M6 earthquake and the December swarm. The rest of the clusters that are west of Zone 4 are merged into Zone 5 because of their intense seismicity during the December swarm but showing no clear response to the M6 earthquake. Characteristics of the five zones are detailed below from east to west.

4.1. Zone 1: Eastern Locked Zone

The easternmost G3 segment (Zone 1) connects to an ITSC, and Zone 1 spans about 30 km along strike (Figure 4). For the past two decades, there were 11 M5–6 earthquakes occurring every 5–6 years in Zone 1 (Shi et al., 2021; Wolfson-Schwehr & Boettcher, 2019). Most of the microearthquakes in the region have local magnitudes less than 3 (Figure S9 in Supporting Information S1). These events are located deeper than 4 km, roughly forming two separate layers. Earthquakes in the shallow layer (4–7 km) organize into sporadic patches along strike, while earthquakes in the deep layer (7–10 km) concentrate at ∼9 km depth forming a continuous linear streak along strike (Figure 4). In conjunction with the spatial pattern, the temporal characteristics of earthquakes in Zone 1 suggest that they can be divided into two groups. The first group includes the shallow layer of seismicity and the easternmost patch of earthquakes (including events deeper than 7 km), which has a near-constant seismicity rate (Group 1, Figure 4c). The second group contains most of the deep-layer earthquakes, and they occur as intermittent bursts during the OBS deployment period (Group 2, Figure 4d), with each burst lasting for about ∼2 days. Here, we refer a seismic burst as a group of microearthquakes striking in limited space and time that can include both mainshock–aftershock sequences and swarms which do not have clear mainshocks (Vidale & Shearer, 2006).

4.2. Zone 2: Barrier Zone

Adjacent to Zone 1, Zone 2 extends 10 km westward to the eastern M6 rupture zone (Figure 5). Zone 2 was denoted as the barrier zone in McGuire et al. (2012) as this fault segment may have involved in both nucleating and terminating the 2008 M6 Gofar earthquake. The fault segment experienced abundant foreshocks before the M6 mainshock and a sudden shutdown of seismicity after the M6 mainshock. Earthquakes in Zone 2 are fragmented into two layers along dip (depth). From seafloor morphological features, these two layers may represent two fault branches. The shallow-layer earthquakes are located in between 2 and 6 km. Seismicity in the shallow

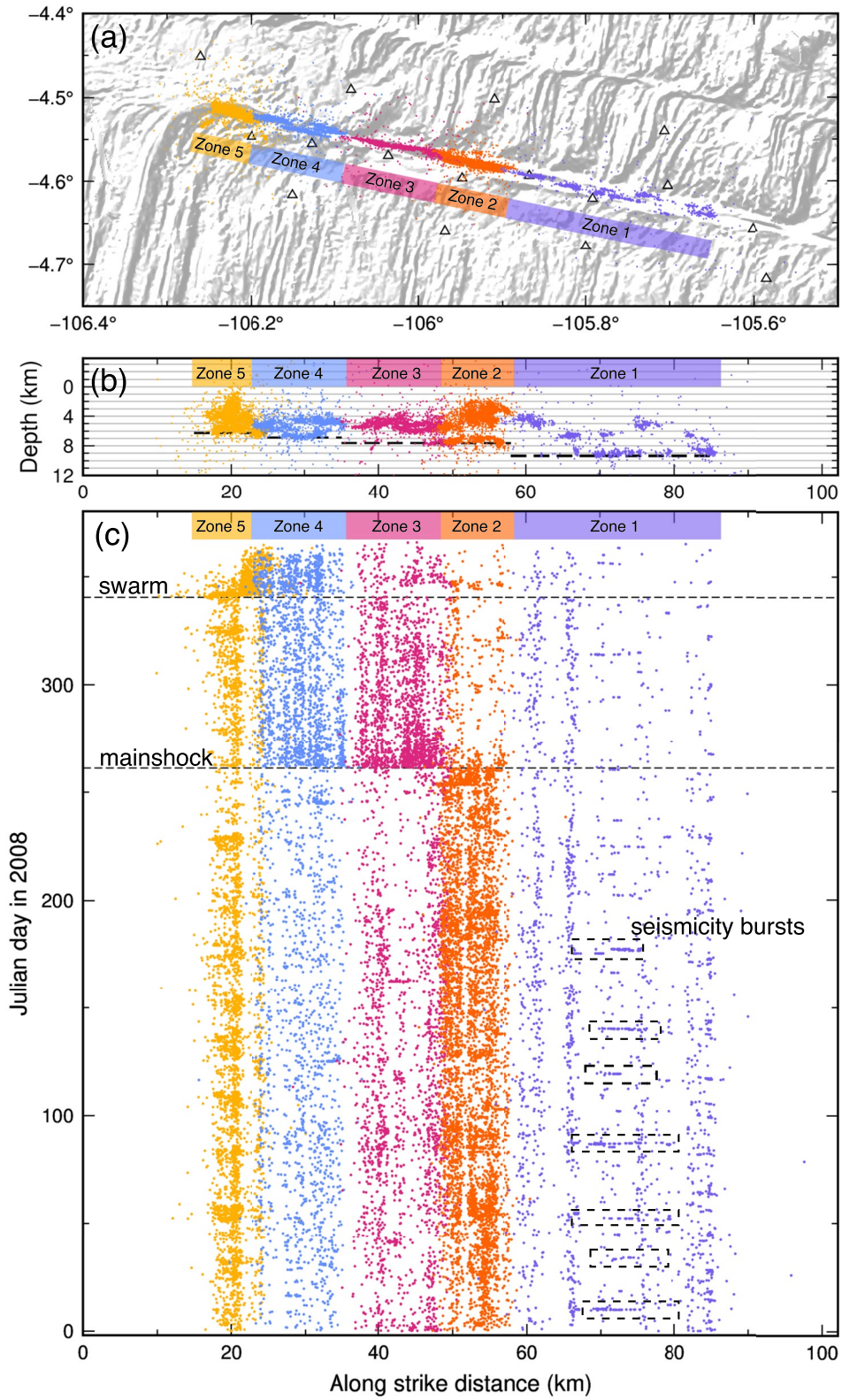

Figure 3. Spatiotemporal evolution of Gofar G3 microearthquakes. (a, b) Map and depth views of earthquakes in the five fault zones. Black dash lines in (b) denote 95% earthquake depth extents of each zone. (c) Spatiotemporal evolution of earthquakes in the five zones. The occurrence times of the M6 mainshock and the December swarm are denoted by black dash lines. Example seismicity bursts in Zone 1 are highlighted by dash-line rectangles.

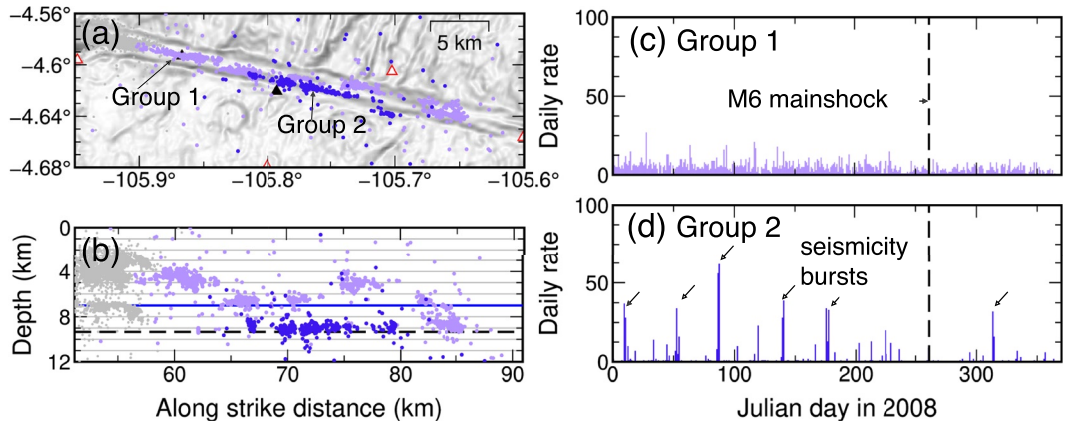

Figure 4. Earthquakes in Zone 1. (a, b) Map and depth views of earthquakes in Zone 1. Different colors indicate two groups of the earthquakes. Blue line in (b) denotes the 7 km depth. Black dash line in (b) denotes the 95% seismicity depth, 9.3 km. (c, d) Temporal evolution of earthquakes in Groups 1 and 2 of Zone 1. Seismicity bursts are marked with black arrows. Black dash line in (c)–(d) denotes the occurrence time of the M6 mainshock.

layer was energetic prior to the M6 mainshock but absent after the mainshock. There was also a 7-day foreshock sequence in the shallow layer, including three $M \sim 4$ foreshocks (Figure 5b and Figure S8 in Supporting Information S1). These shallow-layer earthquakes are termed as the Group 1 events of Zone 2. The deep-layer earthquakes are located in between 7 and 8 km and these events can be further divided into two groups (Groups 2 and 3, Figure 5). Group 2 is adjacent to the mainshock zone and its seismicity shows a similar temporal evolution as of Group 1. In contrast, intermittent earthquake bursts occurred in Group 3 before the M6 mainshock and continued after the mainshock, distinguishing itself from the other two groups in Zone 2.

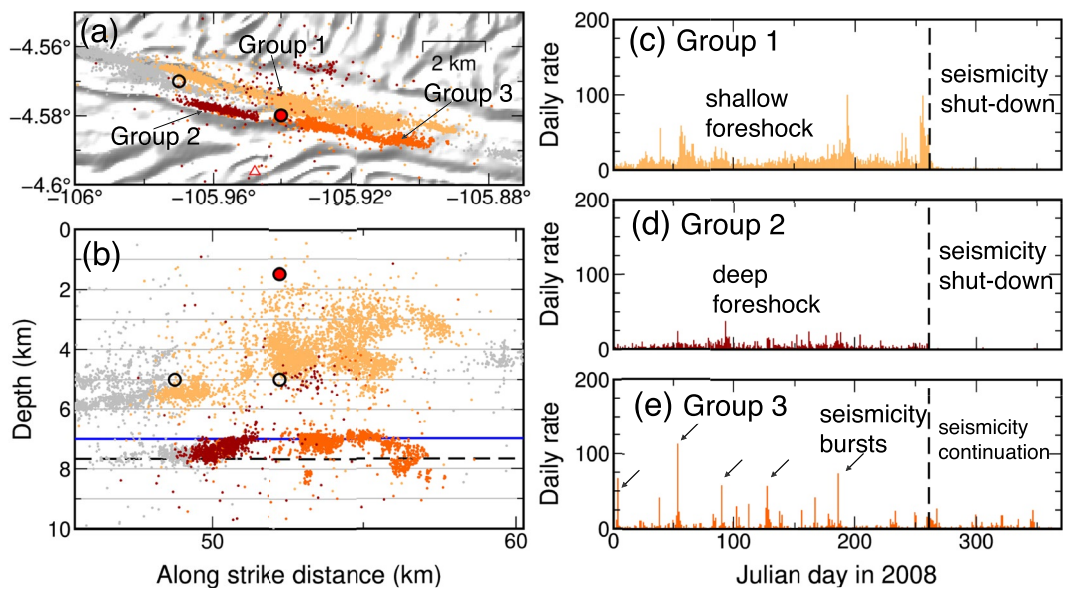

Figure 5. Earthquakes in Zone 2. (a, b) Map and depth views of earthquakes in Zone 2. Different colors indicate different groups of the earthquakes. Red solid circles (depth resolved) and black open circles (depth assigned as 5 km) in (b) denote three $M \sim 4$ events during the 7-day foreshock sequence preceding the M6 mainshock. Blue line in (b) denotes the 7 km depth. Black dash line denotes the 95% seismicity depth, 7.7 km. (c–e) Temporal evolution of earthquakes in the three groups. Seismicity bursts in Group 3 are marked with black arrows. Black dash line in (c)–(e) denotes the occurrence time of the M6 mainshock.

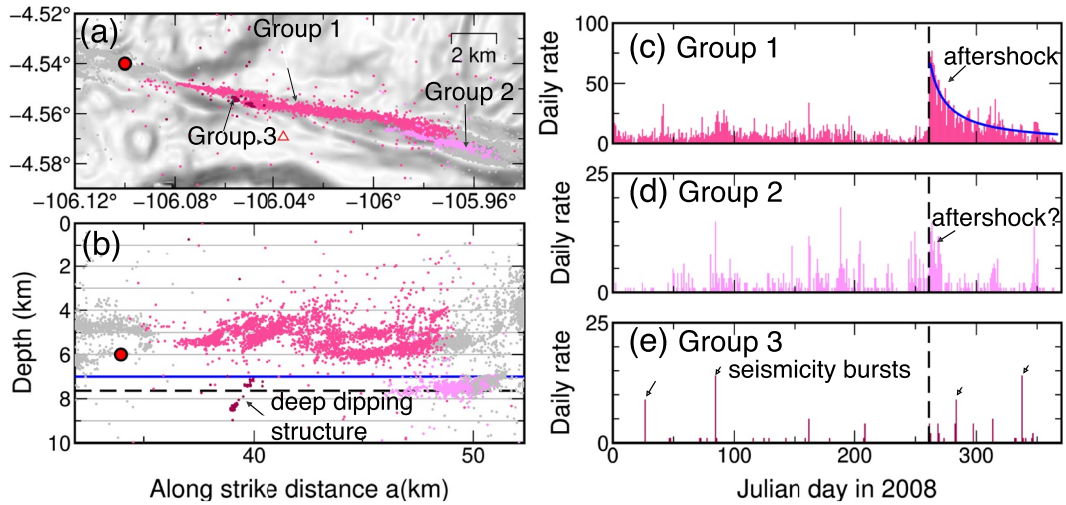

Figure 6. Earthquakes in Zone 3. (a, b) Map and depth views of earthquakes in Zone 3. Different colors indicate different groups of the earthquakes. Red solid circle (depth resolved) in (b) denotes the hypocenter of the M6 mainshock. Blue line in (b) denotes the 7 km depth. Black dash line denotes the 95% seismicity depth, 7.6 km. (c–e) Temporal evolution of earthquakes in the three groups. Aftershocks and seismicity bursts are marked with black arrows in (c)–(e). Aftershocks in Group 1 follow a t^{-1} Omori-decay pattern as shown in (c). Black dash line in (c)–(e) denotes the occurrence time of the M6 mainshock.

4.3. Zone 3: 2008 M6 Mainshock Zone

The 2008 M6 Gofar earthquake occurred in Zone 3, west of Zone 2 (Figure 6). This segment of the Gofar fault is also termed as the mainshock zone in McGuire et al. (2012). Zone 3 extends about 15 km along strike. The M6 mainshock initiated at the western edge of Zone 3 with its epicenter located at 106.1°W/4.54°S at a depth of 6 km. Majority of the earthquakes (80%) in Zone 3 occurred in between 4 and 7 km in depth, forming Group 1 of Zone 3. Group 1 contains most of the aftershocks, which seismicity rate follows a typical Omori-decay pattern (Figure 6c). Earthquakes below 7 km form another two groups of Zone 3, including an eastern streak (Group 2) and a western deep pocket of seismicity (Group 3). Group 2 comprises both short episodes of foreshocks and aftershocks of the mainshock (Figure 6d). Microearthquakes in Group 3 suggest a westward dipping structure between 6 and 8 km, occurring as intermittent bursts (Figure 6e).

4.4. Zone 4: Transition Zone

Zone 4 extends ~12 km west of Zone 3. During the 2008 experiment, the largest aftershock (a M5 event) is located at the western end of Zone 4 (Figure 7). Earthquakes in Zone 4 occurred continuously during the experiment and their activity strongly correlates with both the M6 mainshock in Zone 3 and the December swarm sequence in Zone 5 (Figure 7). Seismicity is distributed in between 4 and 7 km depth without deep earthquakes, forming multiple streaks. Given the seafloor morphological features, seismicity similarity coefficients, and earthquake spatiotemporal patterns, events in Zone 4 are further divided into three groups (Figure 7). These three groups likely originate from three fault strands that are connected by two stepovers, matching seafloor topographic trends (Figure 7a). The active seismicity in Zone 4 lasted for about at least 3 months after the mainshock. The influences of the M6 mainshock from the east and the December swarm sequence from the west correlate with their distances to the three groups (Figures 7c–7e).

4.5. Zone 5: Swarm Zone

The westernmost segment of G3 (Zone 5) connects the transform fault to EPR. There was a surge of earthquakes from 6 to 20 December in 2008 which is termed as the December swarm in McGuire et al. (2012). All earthquakes in Zone 5 are shallower than 7 km and are distributed in between 2 and 6 km in depth. These earthquakes can be divided into two groups based on their temporal behaviors (Figure 8). Group 1 includes quasi-periodic swarms occurring every 24.4 days throughout the year (Figure S11 in Supporting Information S1).

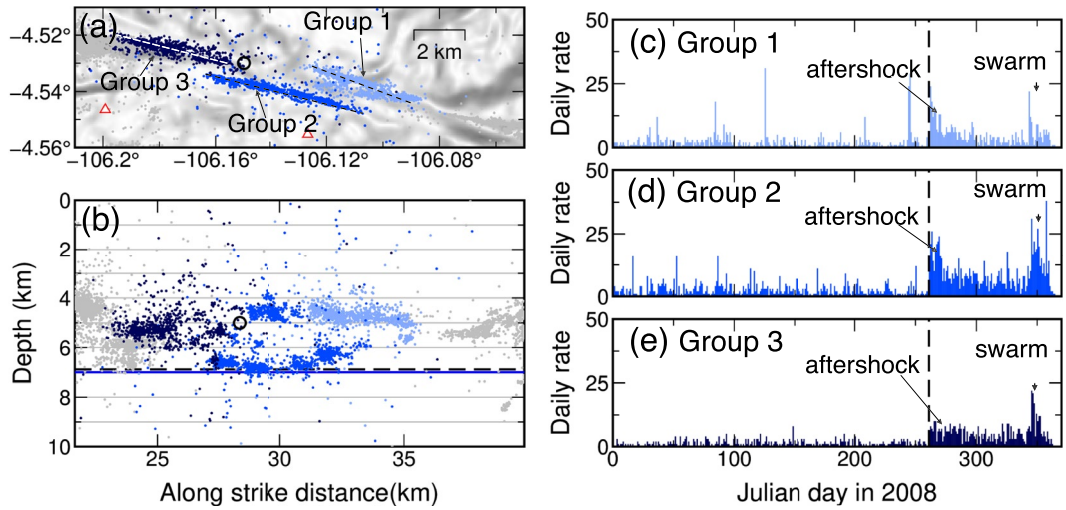

Figure 7. Earthquakes in Zone 4. (a, b) Map and depth views of earthquakes in Zone 4. Different colors indicate different groups of the earthquakes. Dash lines in (a) indicate the inferred fault traces associated with the three earthquake groups of Zone 4. Black open circle in (b) denotes the hypocenter of the M5 aftershock, which depth is assigned at 5 km. Blue line in (b) denotes the 7 km depth. Black dash line denotes the 95% seismicity depth, 6.9 km. (c–e) Temporal evolution of earthquakes in the three groups. Aftershocks and events triggered by the December swarm are marked with black arrows in (c)–(e). Black dash line in (c)–(e) denotes the occurrence time of the M6 mainshock.

The periodicity of these swarms seems to be perturbed by the M6 mainshock in September (Figure 8c). Group 2 is a spatially compact cluster located at ∼5 km depth extending ∼1 km in radius (Figure 8d). Few earthquakes occurred in Group 2 prior to the December swarm, indicating a casual relation between the Group 2 earthquakes and the December swarm.

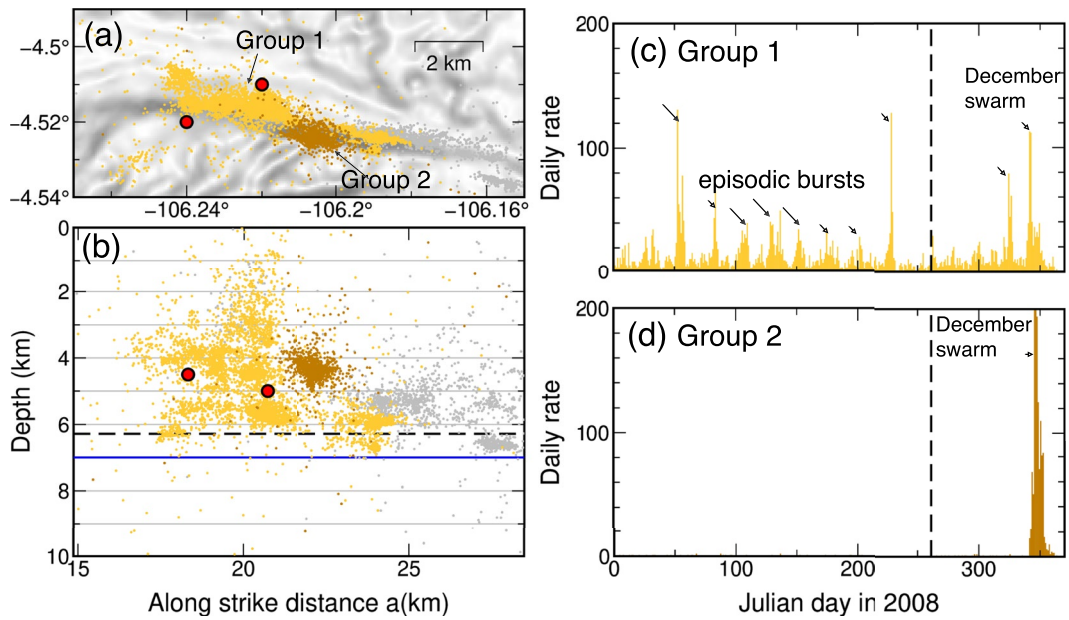

Figure 8. Earthquakes in Zone 5. (a, b) Map and depth views of earthquakes in Zone 5. Different colors indicate different groups of the earthquakes. Red solid circles (depth resolved) in (b) denote the hypocenters of the two M5 events during the December swarm. Blue line in (b) denotes the 7 km depth. Black dash line denotes the 95% seismicity depth, 6.3 km. (c, d) Temporal evolution of earthquakes in the three groups. Swarm events are marked with black arrows in (c)–(d). Black dash lines in (c)–(d) denote the occurrence time of the M6 mainshock.

4.6. Catalog Quality and Uncertainty

Before interpreting the spatiotemporal evolution of the Gofar microseismicity, we first assess the quality of the catalogs and evaluate uncertainties in earthquake locations and their magnitude estimates. Earthquake location uncertainty largely correlates with the network configuration and station coverage. Sensitivity tests of Quebrada earthquake locations suggest that some events outside the OBS network can still be well resolved (Gong et al., 2022). However, their location uncertainties would be greater than those within the network. For instance, the epicenters of events in Zone 2 and Zone 3 (Figures S12 and S13 in Supporting Information S1) have much smaller uncertainties than those of events in Zone 4 and Zone 5 (Figures S13 and S14 in Supporting Information S1), and the difference results from that there was only one functioning station west of Zone 4. Further, earthquake epicenters are better constrained than earthquake depths. For example, the location misfit function (Equation 2) is less sensitive to the earthquake depth than its epicenter (Figures S12–S14 in Supporting Information S1). Given the majority of the earthquakes are shallower than 7 km, there are limited upgoing rays recorded by the given OBS network for the earthquakes, which further affects their depth resolution.

Because of the uncertainty concerns, we aim to obtain the most robust locations. We used the conservative version of EQTransformer that prioritizes minimizing false positives detections (Mousavi et al., 2020). As OBS signals are different from the onshore stations, that is, emergent body wave onsets, the conservative autopicker may have discarded some *P* and *S* picks (García et al., 2022). The COMPLOC location step iteratively examines earthquakes that are potentially shallower than 1 km, and the approach removes 35% of the detected and associated earthquakes. The iterative procedure mostly discards events with fewer phase picks (e.g., less than five *P*/*S* picks), but may also remove events with sufficient phase picks if their depths are not constrained. The GrowClust relocation step uses ℓ_1 norm to evaluate the misfit in differential traveltimes, and it is insensitive to outlier measurements that may be due to cycle skipping in cross correlations (Trugman & Shearer, 2017). Ultimately, our strict quality control criteria would reject earthquakes that can be detected and even located but with large spatial uncertainties. Consequentially, we expect the automated catalog to miss many events.

Interestingly, many $M_L > 3$ events are missed in the automated catalog. The manual catalog contributes 76% of the total $M_L > 3$ events in the combined catalog. It is possible that EQTransformer has difficulties in picking *P* and *S* phases for larger earthquakes (e.g., García et al., 2022; Yoon et al., 2021). Limited by the existing seismic networks, only a small portion of the training data set for EQTransformer is from near-field stations close to large magnitude events, which might be a cause of the picking difficulties. Additionally, the training data set of EQTransformer currently does not include OBS data, which may further hinder its performance. Events in the manual catalog are mostly in the magnitude range of 1.1–4.7 (empirically corrected magnitude). We find that the majority of the manual catalog events are identified during intense seismicity sequences (red circles in Figure S9b in Supporting Information S1), including the December swarm, mainshock–aftershock sequence, and the 1-week-long foreshock in the barrier zone. Earthquakes in these active sequences may have been masked by coda waves from preceding events and cause challenges in identifying their body wave phases using EQTransformer. Therefore, the manual catalog can augment the automated catalog in detecting and locating earthquakes at Gofar.

The strict selection criteria also implies that most of the earthquakes in our catalogs do not have magnitude estimates. For example, only ∼20% earthquakes of the GrowClust catalog have magnitude estimates, and the remaining ∼80% earthquakes did not generate clear waveforms that can pass the selection criteria detailed above. Therefore, the results imply that the apparent magnitude–frequency distribution may be skewed, and the associated *b*-values are perhaps biased toward low values. We caution directly interpreting the *b*-values of the catalogs, and careful investigations on the Gofar earthquake magnitude–frequency distribution are warranted in future follow-up studies. Nevertheless, the continuous seismic data were uniformly processed, the catalogs are examined consistently, and our procedures likely have identified most of the robust earthquakes, particularly, $M > 4$ events.

5. Discussion

The westernmost branch of the Gofar transform fault system (G3) is segmented into five distinct zones along strike, and their seismicity characteristics indicate that different zones might operate under different stress states and have different geometric, material, and mechanical properties. In addition, along-dip segmentation and deep

seismicity seem to be a common feature of the eastern part of G3, including Zones 1–3, although their temporal behaviors differ from zone to zone. Further, seismicity in different zones seems to correlate with each other and may relate to fault slips of adjacent segments. Building upon these observations, we first discuss the along-strike segmentation of G3 and the associated implications in fault slip modes in Section 5.1. We sequentially discuss the locked fault patches, the barrier zone, and the fault zone connects the Gofar fault to EPR. The along-dip segmentation is then discussed comparatively among the fault zones in Section 5.2, including exploring possible controlling mechanisms of the upper-mantle seismicity. We finally infer potential physical processes that may have caused the observed fault interactions (Section 5.3).

5.1. Along-Strike Segmentation of the Westernmost Gofar Transform Fault

5.1.1. Zones 1, 3, and 4: Sporadic Locked Fault Patches

Characteristic M6 earthquakes have repeatedly ruptured Zones 1 and 3 for the past few decades with the 2008 M6 Gofar earthquake rupturing Zone 3 (McGuire et al., 2012; Shi et al., 2021). Microearthquakes are absent in the shallow portions (≤4 km) of these two zones with most of the seismicity located in between 4 and 7 km in depth (Figures 4 and 6). Seismicity delineates linear features that agree well with the surface fault traces, suggesting relatively simple fault-zone structures along strike. Therefore, plate motion is likely, primarily accommodated by seismic slip at these two zones. In this case, the crustal portions of the fault patches are locked during the interseismic period with few microearthquakes, which downdip edges are contoured by microseismicity in the lower crust (4–7 km). Such seismicity distributions are similar to some locked continental faults that aftershocks primarily surround the mainshock rupture areas (Brocher et al., 2015; Chan & Stein, 2009).

Spatial footprint of the aftershocks can be used to estimate the rupture area of the M6 mainshock (e.g., Neo et al., 2021). In conjunction with the M6 epicenter, the aftershock locations indicate that the M6 mainshock primarily ruptured eastward. Such a rupture scenario matches the observed velocity anomaly distribution in Guo et al. (2018) that the mainshock zone is characterized as a low Vp/Vs ratio zone (~1.85) comparing to its neighbor segments (Vp/Vs ratios, ~1.9–2.1), indicating more intact rocks in the mainshock zone. However, the largest aftershock occurred in Zone 4. Additionally, the increased seismicity in Zone 4 after the M6 mainshock suggests that its rupture may have propagated westward as well. In this case, the M6 mainshock might have ruptured bilaterally. Given the uncertainties in the mainshock rupture scenario, there is a range of the possible rupture areas (Figure S10 in Supporting Information S1). The minimum rupture area would extend from the M6 epicenter to the eastern end of Zone 3 with a depth range from 0 to 4 km, which yields a total rupture area of ~60 km^2, an averaged slip distance of 0.60 m and a stress drop of ~3 MPa assuming a rectangular rupture model (Figure S10 in Supporting Information S1). The maximum rupture area would include both Zone 3 and Zone 4 with a depth range of 0–6 km, which yields a total rupture area of ~150 km^2, an averaged slip distance of 0.24 m and a stress drop of ~0.8 MPa. The low stress-drop estimate would be in agreement with those in Moyer et al. (2018) that the stress-drop estimates of earthquakes in the mainshock zone are in between 0.2 and 1 MPa.

There are three apparent fault branches in Zone 4 with an average fault length of ~5 km and an average separation distance of ~1 km (Figure 7). Similar to Zones 1 and 3, there is a lack of seismicity in the shallow portion of the faults (≤4 km), and most microearthquakes likely occurred at the lower-crust depth (4–7 km). The largest aftershock of the 2008 mainshock, a M5 event, likely ruptured one of the three fault branches. The observations suggest that Zone 4 shares similarities with Zones 1 and 3 with plate motion primarily accommodated by seismic slips. However, its fault architecture has three subparallel strands and is more complex than those of Zones 1 and 3. The fault dimension likely controls the nominal magnitude of earthquakes in Zone 4 (Wolfson-Schwehr & Boettcher, 2019). Further, the geometric complexity of the three-fault network may have posed a western rupture boundary for M6 earthquakes in Zone 3, for example, preventing the 2008 mainshock to propagate westward. However, the short stepovers are less than 5 km and they cannot stop an energetic rupture propagation (Barka & Kadinsky-Cade, 1988; Harris & Day, 1999; Wesnousky, 2008). If the mainshock rupture failed to propagate westward (the minimum rupture area scenario), additional mechanical or material variations between Zones 3 and 4 might have contributed to preventing M6 earthquakes rupturing into Zone 4.

5.1.2. Zone 2: Fault Damage Zone Separating Locked Patches

We record intense earthquake activity in Zone 2 starting from the beginning of the 2008 OBS deployment, which abruptly shut down after the M6 mainshock (Figure 5). The mainshock was preceded by a foreshock sequence

in the Zone 2 seven days before its occurrence which includes three $M \sim 4$ earthquakes. There have never been a $M \geq 5$ earthquake rupturing Zone 2 over the past two decades (Shi et al., 2021). Earthquakes spread out the whole crust in the segment from shallow to deep (2–8 km). Roland et al. (2012) show a wide damage zone (~6 km strike-normal direction) across Zone 2 extending through the oceanic crust and penetrating into the upper-most mantle with a ~10%–20% P wave velocity reduction. Such a damage zone differs strikingly from the fault-zone structures of fully coupled mainshock zones, for example, Zone 3 (Froment et al., 2014). The significant velocity reduction is most likely caused by enhanced seawater infiltration with fluid-filled porosity up to 8% (Froment et al., 2014; Roland et al., 2012). These characteristics suggest that the fault segment has pervasive fluid pathways and is embedded with small asperities that could only have $M < 5$ earthquakes. The Zone 2 fault segment likely slips aseismically to accommodate the plate deformation (Figure 10; McGuire et al., 2012; Wolfson-Schwehr & Boettcher, 2019).

The Zone 2 fault segment likely participated in both initiating and terminating the 2008 M6 earthquake, therefore, it is denoted as the barrier zone of G3 (McGuire et al., 2012). Given the damaged zone is filled with fluid with an abundant supply, its high porosity would lead to a strong dilatancy effect, which strengthening may have effectively stabilized the eastward rupture of the M6 earthquake (Y. Liu et al., 2020). Moreover, such dilatancy strengthening effects may also result in generating aseismic transients episodically in Zone 2, which may have accelerated the mainshock fault patch and led to the eventual rupture (Y. Liu et al., 2020). Such a model predicts seismic swarms driven by aseismic slip transients in Zone 2, and we observe a few swarm-like microseismicity sequences in the region that might reflect such transient slips (Figure 5). The dilatancy effects can enable the barrier zone to nucleate and stop earthquake ruptures in the adjacent locked zones.

The halt of crustal seismicity in Zone 2 after the M6 mainshock is perplexing. As predicted by the dilatancy model, the M6 mainshock would promote aseismic slips in the barrier zone, which would cause microseismicity in the region (Y. Liu et al., 2020). Additionally, static Coulomb stresses due to the M6 mainshock would increase in Zone 2, which should also encourage microseismicity (Figure S10 in Supporting Information S1). If dilatancy has played a role in the seismicity shutdown, its effects in porosity increase (pore-pressure drop) must be greater than those from the dilatancy-induced aseismic slips or Coulomb stress changes such that the effective normal stress increase from the pore-pressure drop provides a stronger clamping effects in reducing microearthquake activity in the barrier zone. Another possibility is that the accumulated strains in the barrier zone were temporarily depleted after the M6 mainshock, which would naturally cause a lack of seismicity in the barrier zone. Such a scenario is similar to the "asperity model" proposed in Aki (1984) that the mainshock patches are persistent asperities and the barrier zone slips smoothly during interseismic periods. In this case, limited strain would have accumulated in the barrier zone during the interseismic period. The dilatancy-induced clamping and the stress depletion could have both contributed to halting the seismicity after the M6 earthquake.

The boundaries between Zone 2 and Zones 1 and 3 are remarkably sharp as suggested by the seismicity shutdown after the M6 mainshock (Figure 5), which is different from continental transform faults. For example, the creeping and locked sections of the central San Andreas Fault are connected by a ~20 km transition zone with its seismicity rate tapering toward the locked section (Y. K. Liu et al., 2022). The sharp boundaries of Zone 2 could represent geometric complexities as a bend of seismicity trend in between Zones 2 and 3 is observed in our relocated catalog and also in Froment et al. (2014). This transitional bend situates in a deep valley (Figure 1), which suggests a local strike-normal extension (Gregg et al., 2006; Pockalny et al., 1996). Therefore, the barrier zone may have multiple geometrically confined fault strands that connect to the two locked zones. The geometric complexities might not have played as important a role as dilatancy effects in limiting the M6 mainshock rupture, but their spatial confinement may relate to the sharp boundaries of microseismicity in the barrier zone. Future investigations of seafloor morphology using high-resolution bathymetry data would shed new insights into the fault architecture of the barrier zone.

The fault-zone materials of the barrier zone are likely different from those of the locked zones (Froment et al., 2014; Guo et al., 2018; McGuire et al., 2012; Roland et al., 2012). Such along-strike variations in the fault-zone structures have been observed at other OTFs (Grevemeyer et al., 2021; Maia, 2019; Pockalny et al., 1996; Ren et al., 2022; Searle, 1986; Whitmarsh & Calvert, 1986). The material variations at different Gofar segments likely associate with hydrothermal circulations, and the onsets of developing such variations may have been subjected to secondary tectonic processes, such as dike intrusion, plate motion changes, and jump of ridge positions (Grevemeyer et al., 2021; Maia et al., 2016; Mammerickx & Sandwell, 1986; Pockalny

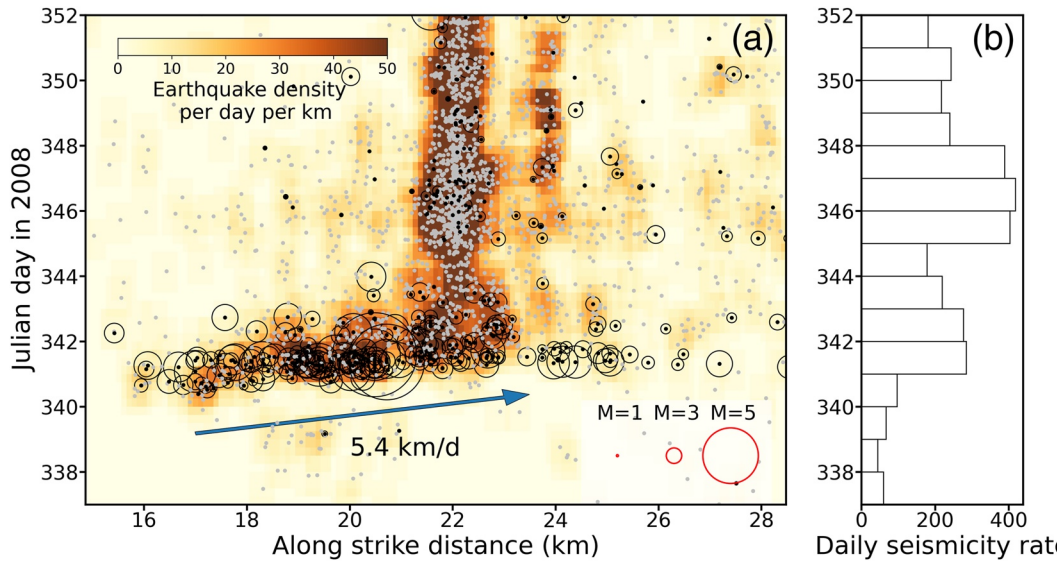

Figure 9. December swarm in Zone 5. (a) Spatiotemporal evolution of the December swarm. Background color denotes earthquake density (km^{-1} day^{-1}). Gray dots denote earthquakes without magnitude estimates. Black dots denote earthquakes having magnitude estimates with their open circle radii showing the earthquake magnitudes. Blue arrow denotes the inferred migration direction of the swarm. (b) Daily seismicity rate of the December swarm in Zone 5.

et al., 1996; Tebbens & Cande, 1997). These processes can couple with enhanced seawater infiltration, forming a positive feedback to promote developing damage zones (e.g., Zone 2). The internal fault structure of Zone 2 shares some similarity with that of Zone 4, and the barrier zone may represent a more evolved stage of Zone 4 with a higher degree of fractures.

5.1.3. Zone 5: Ridge and Transform Fault Interactions

Most of the earthquakes in Zone 5 occurred in the crust with some nearly extending to the seafloor (Figure 8). No M6 earthquake has ruptured this fault segment for the past two decade (Shi et al., 2021). The widespread seismicity and the lack of M6 earthquakes suggest that Zone 5 is also a damage zone and can potentially serve as a barrier zone to influence seismicity in Zone 4. Similar to Zone 2, this fault segment is likely fully saturated with seawater, and fluid may have played a primary role in modulating earthquakes in the segment. Consequentially, dilatancy effects are expected to be strong and aseismic slip may predominantly release the accumulated tectonic stress in Zone 5. However, the fault segment differs from Zone 2 in two major aspects: almost all earthquakes occurred in the crust and there were quasi-periodic earthquake swarms occurring throughout the 2008 experiment.

Spectral analysis of the daily seismicity rate indicates that the swarms in Zone 5 have a recurrence interval of ~24.4 days (Figure S11 in Supporting Information S1). Particularly, an intense swarm of 2,096 events occurred in December, lasting up to two weeks. The December swarm likely initiated around 6 December 2008 11:00 UTC from the western end of the transform fault and migrated toward the east with an average propagation speed of 5.4 km per day (Figure 9). This swarm includes two M5 earthquakes that occurred at 7 December 2008 08:53:22 UTC and 7 December 2008 14:15:31 UTC (Figure S9 in Supporting Information S1). Most of the large magnitude events occurred during the first 2 days of the swarm (Figure 9), and several $M \geq 2$ events also occurred in Zone 4 as part of the sequence (Figure 9). The swarm broke a fault patch that was previously quiescent, resulting in 823 microearthquakes within a 2 km footprint for 12 days. We consider this December sequence as a swarm instead of a foreshock–mainshock–aftershock sequence because of the clear migration pattern and the seismicity rate pattern that there was no single dominant earthquake as an obvious mainshock.

The depth limit in earthquakes and the quasi-periodic swarms likely reflect influences from the spreading center. The Zone 5 segment is at the intersection between the ridge and transform fault, and the thermal structure will favor a shallow downdip edge of the seismogenic zone (Roland et al., 2010). Further, the periodic swarms might be related to magma and fluid activity or transient slip events. The swarm periodicity does not match the semi-diurnal ocean tides that are known to trigger earthquakes at EPR (Stroup et al., 2007, 2009). The anomalistic

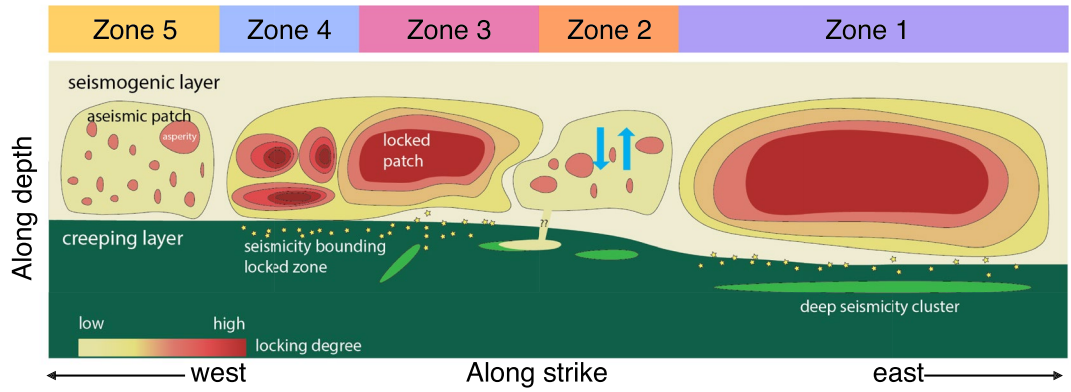

Figure 10. Conceptual model of microseismicity and fault slip modes at the westernmost Gofar transform fault. Irregular shaped patches denote fault patches of various sizes, and their colors correspond to different locking degrees. Zones 1, 3, and 4 are represented as sporadic, locked patches. Zones 2 and 5 are represented as damage zones embedded with small asperities. Microseismicity near the Moho discontinuity is denoted as small yellow stars. Green and yellow ellipses denote deep seismicity clusters. Blue arrows denote intense fluid circulation in Zone 2.

month tide has a cycle of 27.5 days and it may not relate to the observed swarms since its period is longer than that of the Zone 5 swarms. Magma chamber activity can couple with tidal stresses to modulate seismicity of near-ridge faults (Scholz et al., 2019). Therefore, the swarms could be due to combined effects of magma activity and tidal stresses. Additionally, fluid pockets and pathways in the fault zone may experience frequent recharge and discharge processes, leading to periodic fluid migration episodes, which can also produce similar swarms at various spatiotemporal scales (Ross & Cochran, 2021; Ross et al., 2020). There was a temporary pause of the periodic swarms soon after the M6 mainshock (Figure 8). We speculate that the pause might relate to triggered aseismic slips in Zone 5 due to the M6 mainshock. The triggered aseismic slips would promote a temporary porosity increase and cause a pore-pressure decrease (Y. Liu et al., 2020). Such a process would clamp the fault (dilatancy effects) and discourage microearthquakes. The pore-pressure drop eventually recovered as suggested by the seismicity (Figure 8), which may have been assisted by intense hydrothermal circulation in the damaged fault zone due to its proximity to the ridge. If this scenario holds true, fluid migration and hydrothermal circulation may be the primary cause of the Zone 5 swarms.

The fault patch of Group 2 earthquakes in Zone 5 likely represents a different fault strand than that had the M5 doublet and the rest of the December swarm (Group 1). The fault strand may have been surrounded by barriers that were broken by the M5 earthquakes, and the influx of fluid may have caused the intense swarm. Such a hypothesis is supported by the lack of earthquake similarities between the two groups in Zone 5 and the absence of events prior to the December swarm. The current bathymetry data cannot distinguish possible seafloor morphological features related to the fault strand of the Group 2 earthquakes, but the ridge–transform connection likely produces a complex, heterogeneous fault network, such as indicated by the prominent "J"-shape structure of EPR.

5.2. Deep Earthquakes, Fluid–Rock Interaction, and Upper-Mantle Thermal Structure

Depth extent of microseismicity decreases from east to west along the westernmost Gofar transform fault as indicated by the 95 percentile seismicity depth of its five segments (Figure 3). The nominal depth extent of OTF seismicity is primarily controlled by the position of the 600°C isotherm (Abercrombie & Ekström, 2001; Behn et al., 2007; Bergman & Solomon, 1988; Boettcher et al., 2007; Braunmiller & Nábělek, 2008; Roland et al., 2010). At Gofar, the 600°C isotherm is likely above or near the crust–mantle boundary at ~7 km (Roland et al., 2010), which would create a narrow layer of aftershock near Moho that separates the locked layer in the crust from free creeping layer in the mantle, such as the events of Group 1 in Zone 3 (Figures 6c and 10). Microearthquakes also occur in the upper mantle at the eastern G3 (Zones 1–3) from 7 to 10 km, including Group 2 in Zone 1 (Figure 4d), Groups 2 and 3 in Zone 2 (Figures 5d and 5e), and Groups 2 and 3 in Zone 3 (Figures 6d and 6e). These deep seismicity is consistent with previous earthquake location results albeit at shallower depths (Guo et al., 2018; McGuire et al., 2012). Comparing to EPR, the ITSC likely has less magma

supply and a lower temperature (Pickle et al., 2009). The deepening of the 95% seismicity depth could indicate an upper-mantle thermal structure with the 600°C isotherm deepening from west (EPR) to east (ITSC). However, such an isotherm transition would occur gradually over a large spatial extent in contrast to our observed staircase-changes (Figure 3). Furthermore, an isotherm deepening alone cannot explain the depth gaps between two layers of seismicity in Zones 1–3 (Figures 4–6 and 10).

Fluid–rock interaction would also generate earthquakes below the expected 600°C isotherm (Kohli & Warren, 2020; Kuna et al., 2019; Yu et al., 2021). As the barrier zone (Zone 2) centers at the eastern section of G3, its fractures would lead to enhanced permeability within and around the segment, promote hydrothermal circulation to the upper mantle, and lower the ambient mantle temperature (Kohli & Warren, 2020). Such fluid–rock interactions would alter the minerals and promote seismicity in the upper mantle (Prigent et al., 2020). Further, fractures in the high temperature peridotite mylonites (≥800°C) and coarse-grained peridotite are capable to host brittle failures at ambient mantle temperature conditions (Figure 10; Kohli et al., 2021; Prigent et al., 2020; Yu et al., 2021). For example, deep seismicity at the Romanche transform fault can occur down to 30 km depth, which would be in a temperature range of 700°C–900°C (Yu et al., 2021). These two mechanisms are not exclusive, and they both enable strain to localize at deeper depth beyond the Moho discontinuity. Finally, fluid–rock interaction can couple with the upper-mantle thermal structure to promote deep seismicity in eastern G3 (Figure 10).

The temporal behaviors of deep microseismicity vary from patch to patch, indicating that their physical drivers are likely dissimilar. For example, intermittent seismicity bursts are observed at Group 2 in Zone 1, Group 3 in Zone 2, and Group 3 of Zone 3 (Figures 4d, 5e, and 6e). These bursts do not seem to be strongly influenced by the 2008 M6 mainshock. Most of the seismicity bursts are not mainshock–aftershock sequences. Therefore, they may be more likely related to episodic fluid activity or transient slips. Similar two layers of seismicity are observed at the Blanco transform fault with the deep layer in the upper mantle at 13 km depth migrating as swarms, which were likely driven by creeps partially and episodically (Kuna et al., 2019). In contrast, the deep bursts at Gofar do not have clear migration patterns, suggesting that their driving forces are likely local. Another class of deep seismicity occurred continuously throughout the year and their temporal behaviors correlate the M6 mainshock. For example, Group 2 in Zone 2 suddenly paused after the mainshock (Figure 5d), similar to the shallow seismicity in the barrier zone, indicating possible connections between the fault patches (Figure 10). Earthquakes of Group 2 in Zone 3 also correlate with the M6 mainshock with an apparent increase in seismicity after the M6 mainshock, which might have been affected by its afterslip (Figure 6d).

5.3. Fault Interaction

Different Gofar fault segments actively interact with each other and yield correlated seismic activities. The barrier zone may have regulated the M6 mainshock in both its rupture nucleation and termination (Figure 5). The M6 mainshock paused seismicity in the barrier zone (Figure 5) and disturbed the quasi-periodic swarms in the Zone 5 (Figure 8). Earthquakes in Zone 4 are strongly influenced by both the M6 mainshock in Zone 3 and the December swarm in Zone 5 (Figure 7). The microseismicity rate in Zone 4 increased after the M6 mainshock and remained at a higher-than-background level for about 3 months. The December swarm caused another surge of seismicity in Zone 4, lasting till the end of the experiment. These earthquakes are likely triggered by the mainshock and the December swarm. The lengthy duration (4 months) indicates that nonlinear triggering mechanisms might have controlled the triggered seismicity. For example, the M6 mainshock may have caused afterslip, viscoelastic relaxation, or poroelastic relaxation at the crust–mantle boundary, driving the triggered seismicity (Marone et al., 1991; Savage & Prescott, 1978; Segall & Lu, 2015). The December swarm might represent a transient aseismic slip event propagating from west to east, causing the surge of seismicity in Zone 4 (Figure 9). Alternatively, fluid migration could have also caused the long-lasting triggered sequences (Ross & Cochran, 2021; Ross et al., 2020). In this case, the lower crust may have pervasive fluid pathways. The high sensitivity of Zone 4 to adjacent fault patches and its complex fault architecture suggest that Zone 4 might be a transition zone with a mélange locking structure in between predominantly seismic (Zone 3) and aseismic (Zone 5) fault segments.

These interactions likely involve multiple concurrent physical processes that may facilitate each other to fabricate the observed complex seismicity evolution at Gofar. For example, stress triggering due to the dynamic and static stress changes could cause aseismic slips or transients, which may interact with the fluid-driven seismicity at various fault patches (Kaven, 2020; Ross et al., 2020; Shelly et al., 2011; van der Elst et al., 2013). We infer that complex architecture, material property variation, and intense seawater infiltration would cause stress

heterogeneity and stimulate prevalent aseismic slips. Such aseismic slips could propagate over a large range episodically, bridging along-strike and along-dip fault interactions. The highly heterogeneous stress field is sensitive to perturbations either from passing seismic waves, transients, or fluid migrations (Cattania et al., 2017; Ross et al., 2020; Shelly et al., 2011). The complex fault architecture and material variation can collectively produce geometric and mechanical fault segmentation, which are reflected in the complex seismicity evolution.

6. Conclusions

We detect, locate, and relocate 30,854 earthquakes at the westernmost Gofar transform fault using a 1-year OBS data collected in 2008. The microearthquakes have complex spatiotemporal patterns, suggesting five distinct segments along strike of the transform fault. We find the following:

1. Two locked fault patches that can have characteristic M6 earthquakes are distributed within the oceanic crust with their downdip edges marked by microearthquakes.
2. Two damage zones have microearthquakes spreading out the whole oceanic crust.
3. The locked fault segments have simple fault geometries while the damage zones are likely composed of multiple strands.
4. Episodic seismicity bursts frequently occur in Zone 5 that connects the transform fault to the East Pacific Rise.
5. Deep seismicity in the upper mantle is observed at the eastern section of the transform fault up to 10 km, often as intermittent seismicity bursts.

Taking microseismicity as a proxy of the fault slip mode, we infer the following:

1. The primary slip mode varies from segment to segment, but the seismic and aseismic slip modes are not exclusive in the same segment, particularly in the down-dip direction.
2. Complex fault architecture likely contributes to the observed segmentation.
3. The damage zones are likely pervasively fractured with enhanced seawater infiltration.
4. Fluid–rock interaction is crucial in controlling slip events in the damage zones and in modulating earthquake ruptures in locked zones.
5. Multiple physical processes may concur and cause the fault segments interact with each other, producing the complex seismicity pattern.

Data Availability Statement

The seismic data are available from the Data Management Center (DMC) of the Incorporated Research Institutions for Seismology (IRIS) under the network codes ZD (https://www.fdsn.org/networks/detail/ZD_2007/). IRIS Data Services and the IRIS DMC were used to access waveforms, related metadata, and derived products used in this study. IRIS Data Services are funded through the Seismological Facilities for the Advancement of Geoscience and EarthScope (SAGE) proposal of the National Science Foundation (NSF) under Cooperative Agreement EAR-1261681. The relocated $M > 5.5$ events are from Shi et al. (2021), available at https://doi.org/10.5281/zenodo.4646438, and the bathymetry data can be obtained from https://www.ngdc.noaa.gov/maps/autogrid/. We used open-source software EQTransformer (Mousavi et al., 2020), REAL (Zhang et al., 2019), COMPLOC (G. Lin & Shearer, 2006), and GrowClust (Trugman & Shearer, 2017) for earthquake detection, association, location, and relocation. The earthquake catalog is archived at Marine Geoscience Data System, Cruise doi: https://doi.org/10.26022/IEDA/331024 (http://get.iedadata.org/doi/331024).

Acknowledgments
We thank the Editor Rachel Abercrombie, Associate Editor, and two anonymous reviewers for their thoughtful and constructive reviews of the paper. J.G. and W.F. acknowledge support from National Science Foundation (NSF) Grants OCE-1833279 and EAR-2143413. The ocean bottom seismometer instruments were provided by the Ocean Bottom Seismograph Instrument Center (OBSIC). The authors thank Jeffrey McGuire, John Collins, and the rest of the 2008 Quebrada–Discovery–Gofar experiment team for collecting and archiving the data. The authors thank Peter Shearer for teaching us the COMPLOC and GrowClust software and Margaret Boettcher, Yajing Liu, Mark Behn, and Chen Ji for insightful discussions.

References

Abercrombie, R. E., & Ekström, G. (2001). Earthquake slip on oceanic transform faults. *Nature*, *410*(6824), 74–77. https://doi.org/10.1038/35065064

Aderhold, K., & Abercrombie, R. E. (2016). The 2015 Mw 7.1 earthquake on the Charlie–Gibbs transform fault: Repeating earthquakes and multimodal slip on a slow oceanic transform. *Geophysical Research Letters*, *43*, 6119–6128. https://doi.org/10.1002/2016GL068802

Aki, K. (1965). Maximum likelihood estimate of b in the formula $\log n = a - bm$ and its confidence limits. *Bulletin of Earthquake Research Institute, Tokyo University*, *43*, 237–239.

Aki, K. (1984). Asperities, barriers, characteristic earthquakes and strong motion prediction. *Journal of Geophysical Research*, *89*(B7), 5867–5872. https://doi.org/10.1029/JB089iB07p05867

Allen, R. V. (1978). Automatic earthquake recognition and timing from single traces. *Bulletin of the Seismological Society of America*, *68*(5), 1521–1532. https://doi.org/10.1785/BSSA0680051521

Avouac, J.-P. (2015). From geodetic imaging of seismic and aseismic fault slip to dynamic modeling of the seismic cycle. *Annual Review of Earth and Planetary Sciences*, *43*(1), 233–271. https://doi.org/10.1146/annurev-earth-060614-105302

Bakun, W. H., Aagaard, B., Dost, B., Ellsworth, W. L., Hardebeck, J. L., Harris, R. A., et al. (2005). Implications for prediction and hazard assessment from the 2004 Parkfield earthquake. *Nature*, *437*(7061), 969–974. https://doi.org/10.1038/nature04067

Barka, A. A., & Kadinsky-Cade, K. (1988). Strike-slip fault geometry in Turkey and its influence on earthquake activity. *Tectonics*, *7*(3), 663–684. https://doi.org/10.1029/TC007i003p00663

Behn, M. D., Boettcher, M. S., & Hirth, G. (2007). Thermal structure of oceanic transform faults. *Geology*, *35*(4), 307–310. https://doi.org/10.1130/g23112a.1

Bergman, E. A., & Solomon, S. C. (1988). Transform fault earthquakes in the North Atlantic: Source mechanisms and depth of faulting. *Journal of Geophysical Research*, *93*(B8), 9027–9057. https://doi.org/10.1029/JB093iB08p09027

Boettcher, M. S., Hirth, G., & Evans, B. (2007). Olivine friction at the base of oceanic seismogenic zones. *Journal of Geophysical Research*, *112*, B01205. https://doi.org/10.1029/2006JB004301

Boettcher, M. S., & Jordan, T. H. (2004). Earthquake scaling relations for mid-ocean ridge transform faults. *Journal of Geophysical Research*, *109*, B12302. https://doi.org/10.1029/2004JB003110

Bondár, I., & Storchak, D. (2011). Improved location procedures at the international seismological centre. *Geophysical Journal International*, *186*(3), 1220–1244. https://doi.org/10.1111/j.1365-246X.2011.05107.x

Braunmiller, J., & Nábělek, J. (2008). Segmentation of the Blanco Transform Fault Zone from earthquake analysis: Complex tectonics of an oceanic transform fault. *Journal of Geophysical Research*, *113*, B07108. https://doi.org/10.1029/2007JB005213

Brocher, T. M., Baltay, A. S., Hardebeck, J. L., Pollitz, F. F., Murray, J. R., Llenos, A. L., et al. (2015). The Mw 6.0 24 August 2014 South Napa earthquake. *Seismological Research Letters*, *86*(2A), 309–326. https://doi.org/10.1785/0220150004

Castellanos, J. C., Zhan, Z., & Wu, W. (2020). Absolute centroid location of submarine earthquakes from 3D waveform modeling of water reverberations. *Journal of Geophysical Research: Solid Earth*, *125*, e2019JB018941. https://doi.org/10.1029/2019JB018941

Cattania, C., McGuire, J. J., & Collins, J. A. (2017). Dynamic triggering and earthquake swarms on East Pacific Rise transform faults. *Geophysical Research Letters*, *44*, 702–710. https://doi.org/10.1002/2016GL070857

Chan, C.-H., & Stein, R. S. (2009). Stress evolution following the 1999 Chi-Chi, Taiwan, earthquake: Consequences for afterslip, relaxation, aftershocks and departures from Omori decay. *Geophysical Journal International*, *177*(1), 179–192. https://doi.org/10.1111/j.1365-246X.2008.04069.x

Ekström, G., Nettles, M., & Dziewoński, A. (2012). The global CMT project 2004–2010: Centroid-moment tensors for 13,017 earthquakes. *Physics of the Earth and Planetary Interiors*, *200–201*, 1–9. https://doi.org/10.1016/j.pepi.2012.04.002

Freed, A. M. (2005). Earthquake triggering by static, dynamic, and postseismic stress transfer. *Annual Review of Earth and Planetary Sciences*, *33*(1), 335–367. https://doi.org/10.1146/annurev.earth.33.092203.122505

Froment, B., McGuire, J. J., van der Hilst, R. D., Gouédard, P., Roland, E. C., Zhang, H., & Collins, J. A. (2014). Imaging along-strike variations in mechanical properties of the Gofar transform fault, East Pacific Rise. *Journal of Geophysical Research: Solid Earth*, *119*, 7175–7194. https://doi.org/10.1002/2014JB011270

García, J. E., Fernández-Prieto, L. M., Villaseñor, A., Sanz, V., Ammirati, J., Díaz Suárez, E. A., & García, C. (2022). Performance of deep learning pickers in routine network processing applications. *Seismological Research Letters*, *93*(5), 2529–2542. https://doi.org/10.1785/0220210323

Gong, J., Fan, W., & Parnell-Turner, R. (2022). Microseismicity indicates atypical small-scale plate rotation at the Quebrada transform fault system, East Pacific Rise. *Geophysical Research Letters*, *49*, e2021GL097000. https://doi.org/10.1029/2021GL097000

Gregg, P. M., Lin, J., & Smith, D. K. (2006). Segmentation of transform systems on the East Pacific Rise: Implications for earthquake processes at fast-slipping oceanic transform faults. *Geology*, *34*(4), 289–292. https://doi.org/10.1130/g22212.1

Grevemeyer, I., Rüpke, L. H., Morgan, J. P., Iyer, K., & Devey, C. W. (2021). Extensional tectonics and two-stage crustal accretion at oceanic transform faults. *Nature*, *591*(7850), 402–407. https://doi.org/10.1038/s41586-021-03278-9

Guo, H., Zhang, H., & Froment, B. (2018). Structural control on earthquake behaviors revealed by high-resolution Vp/Vs imaging along the Gofar transform fault, East Pacific Rise. *Earth and Planetary Science Letters*, *499*, 243–255. https://doi.org/10.1016/j.epsl.2018.07.037

Han, S., Bangs, N. L., Carbotte, S. M., Saffer, D. M., & Gibson, J. C. (2017). Links between sediment consolidation and Cascadia megathrust slip behaviour. *Nature Geoscience*, *10*(12), 954–959. https://doi.org/10.1038/s41561-017-0007-2

Hardebeck, J. L., Nazareth, J. J., & Hauksson, E. (1998). The static stress change triggering model: Constraints from two Southern California aftershock sequences. *Journal of Geophysical Research*, *103*(B10), 24427–24437. https://doi.org/10.1029/98JB00573

Harris, R. A. (2017). Large earthquakes and creeping faults. *Reviews of Geophysics*, *55*, 169–198. https://doi.org/10.1002/2016RG000539

Harris, R. A., & Day, S. M. (1999). Dynamic 3D simulations of earthquakes on En Echelon Faults. *Geophysical Research Letters*, *26*(14), 2089–2092. https://doi.org/10.1029/1999GL900377

Hicks, S. P., Okuwaki, R., Steinberg, A., Rychert, C. A., Harmon, N., Abercrombie, R. E., et al. (2020). Back-propagating supershear rupture in the 2016 Mw 7.1 Romanche transform fault earthquake. *Nature Geoscience*, *13*(9), 647–653. https://doi.org/10.1038/s41561-020-0619-9

Hsu, Y.-J., Simons, M., Avouac, J.-P., Galetzka, J., Sieh, K., Chlieh, M., et al. (2006). Frictional afterslip following the 2005 Nias–Simeulue earthquake, Sumatra. *Science*, *312*(5782), 1921–1926. https://doi.org/10.1126/science.1126960

Jiang, J., Bock, Y., & Klein, E. (2021). Coevolving early afterslip and aftershock signatures of a San Andreas Fault rupture. *Science Advances*, *7*(15), eabc1606. https://doi.org/10.1126/sciadv.abc1606

Kato, A., Obara, K., Igarashi, T., Tsuruoka, H., Nakagawa, S., & Hirata, N. (2012). Propagation of slow slip leading up to the 2011 M w 9.0 Tohoku-Oki earthquake. *Science*, *335*(6069), 705–708. https://doi.org/10.1126/science.1215141

Kaven, J. O. (2020). Seismicity rate change at the Coso geothermal field following the July 2019 Ridgecrest earthquakes. *Bulletin of the Seismological Society of America*, *110*(4), 1728–1735. https://doi.org/10.1785/0120200017

King, G. C. P., Stein, R. S., & Lin, J. (1994). Static stress changes and the triggering of earthquakes. *Bulletin of the Seismological Society of America*, *84*(3), 935–953. https://doi.org/10.1785/BSSA0840030935

Kohli, A. H., & Warren, J. M. (2020). Evidence for a deep hydrologic cycle on oceanic transform faults. *Journal of Geophysical Research: Solid Earth*, *125*, e2019JB017751. https://doi.org/10.1029/2019JB017751

Kohli, A. H., Wolfson-Schwehr, M., Prigent, C., & Warren, J. M. (2021). Oceanic transform fault seismicity and slip mode influenced by seawater infiltration. *Nature Geoscience*, *14*(8), 606–611. https://doi.org/10.1038/s41561-021-00778-1

Kuna, V. M., Nábělek, J. L., & Braunmiller, J. (2019). Mode of slip and crust–mantle interaction at oceanic transform faults. *Nature Geoscience*, *12*(2), 138–142. https://doi.org/10.1038/s41561-018-0287-1

Lay, T., Kanamori, H., Ammon, C. J., Koper, K. D., Hutko, A. R., Ye, L., et al. (2012). Depth-varying rupture properties of subduction zone megathrust faults. *Journal of Geophysical Research*, *117*, B04311. https://doi.org/10.1029/2011JB009133

Lin, G., & Shearer, P. (2005). Tests of relative earthquake location techniques using synthetic data. *Journal of Geophysical Research*, *110*), B04304. https://doi.org/10.1029/2004JB003380
Lin, G., & Shearer, P. (2006). The COMPLOC earthquake location package. *Seismological Research Letters*, *77*(4), 440–444. https://doi.org/10.1785/gssrl.77.4.440
Lin, J., & Stein, R. S. (2004). Stress triggering in thrust and subduction earthquakes and stress interaction between the southern San Andreas and nearby thrust and strike-slip faults. *Journal of Geophysical Research*, *109*, B02303. https://doi.org/10.1029/2003JB002607
Liu, Y., McGuire, J. J., & Behn, M. D. (2012). Frictional behavior of oceanic transform faults and its influence on earthquake characteristics. *Journal of Geophysical Research*, *117*, B04315. https://doi.org/10.1029/2011JB009025
Liu, Y., McGuire, J. J., & Behn, M. D. (2020). Aseismic transient slip on the Gofar transform fault, East Pacific Rise. *Proceedings of the National Academy of Sciences of the United States of America*, *117*(19), 10188–10194. https://doi.org/10.1073/pnas.1913625117
Liu, Y., & Rice, J. R. (2005). Aseismic slip transients emerge spontaneously in three-dimensional rate and state modeling of subduction earthquake sequences. *Journal of Geophysical Research*, *110*, B08307. https://doi.org/10.1029/2004JB003424
Liu, Y. K., Ross, Z. E., Cochran, E. S., & Lapusta, N. (2022). A unified perspective of seismicity and fault coupling along the San Andreas Fault. *Science Advances*, *8*(8), eabk1167. https://doi.org/10.1126/sciadv.abk1167
Maeda, N. (1985). A method for reading and checking phase times in autoprocessing system of seismic wave data. *Zisin*, *38*, 365–379. https://doi.org/10.4294/zisin1948.38.3_365
Maia, M. (2019). Chapter 3—Topographic and morphologic evidences of deformation at oceanic transform faults: Far-field and local-field stresses. In J. C. Duarte (Ed.), *Transform plate boundaries and fracture zones* (pp. 61–87). Elsevier. https://doi.org/10.1016/B978-0-12-812064-4.00003-7
Maia, M., Sichel, S., Briais, A., Brunelli, D., Ligi, M., Ferreira, N., et al. (2016). Extreme mantle uplift and exhumation along a transpressive transform fault. *Nature Geoscience*, *9*(8), 619–623. https://doi.org/10.1038/ngeo2759
Mammerickx, J., & Sandwell, D. (1986). Rifting of old oceanic lithosphere. *Journal of Geophysical Research*, *91*(B2), 1975–1988. https://doi.org/10.1029/JB091iB02p01975
Marone, C. J., Scholtz, C. H., & Bilham, R. (1991). On the mechanics of earthquake afterslip. *Journal of Geophysical Research*, *96*(B5), 8441–8452. https://doi.org/10.1029/91JB00275
McGuire, J. J. (2008). Seismic cycles and earthquake predictability on East Pacific Rise transform faults. *Bulletin of the Seismological Society of America*, *98*(3), 1067–1084. https://doi.org/10.1785/0120070154
McGuire, J. J., Boettcher, M. S., & Jordan, T. H. (2005). Foreshock sequences and short-term earthquake predictability on East Pacific Rise transform faults. *Nature*, *434*(7032), 457–461. https://doi.org/10.1038/nature03377
McGuire, J. J., Collins, J. A., Gouédard, P., Roland, E., Lizarralde, D., Boettcher, M. S., et al. (2012). Variations in earthquake rupture properties along the Gofar transform fault, East Pacific Rise. *Nature Geoscience*, *5*(5), 336–341. https://doi.org/10.1038/ngeo1454
McLaskey, G. C. (2019). Earthquake initiation from laboratory observations and implications for foreshocks. *Journal of Geophysical Research: Solid Earth*, *124*, 12882–12904. https://doi.org/10.1029/2019JB018363
Mousavi, S. M., Ellsworth, W. L., Zhu, W., Chuang, L. Y., & Beroza, G. C. (2020). Earthquake transformer—An attentive deep-learning model for simultaneous earthquake detection and phase picking. *Nature Communications*, *1*, 3952. https://doi.org/10.1038/s41467-020-17591-w
Mousavi, S. M., Sheng, Y., Zhu, W., & Beroza, G. C. (2019). STanford EArthquake Dataset (STEAD): A global data set of seismic signals for AI. *IEEE Access*, *7*, 179464–179476. https://doi.org/10.1109/ACCESS.2019.2947848
Moyer, P. A., Boettcher, M. S., McGuire, J. J., & Collins, J. A. (2018). Spatial and temporal variations in earthquake stress drop on Gofar transform fault, East Pacific Rise: Implications for fault strength. *Journal of Geophysical Research: Solid Earth*, *123*, 7722–7740. https://doi.org/10.1029/2018JB015942
Neo, J. C., Huang, Y., Yao, D., & Wei, S. (2021). Is the aftershock zone area a good proxy for the mainshock rupture area? *Bulletin of the Seismological Society of America*, *111*(1), 424–438. https://doi.org/10.1785/0120190200
Obara, K., & Kato, A. (2016). Connecting slow earthquakes to huge earthquakes. *Science*, *353*(6296), 253–257. https://doi.org/10.1126/science.aaf1512
Parnell-Turner, R., Smith, D., & Dziak, R. (2022). Hydroacoustic monitoring of seafloor spreading and transform faulting in the equatorial Atlantic Ocean. *Journal of Geophysical Research: Solid Earth*, *127*, e2022JB024008. https://doi.org/10.1029/2022JB024008
Pickle, R. C., Forsyth, D. W., Harmon, N., Nagle, A. N., & Saal, A. (2009). Thermo-mechanical control of axial topography of intra-transform spreading centers. *Earth and Planetary Science Letters*, *284*(3), 343–351. https://doi.org/10.1016/j.epsl.2009.05.004
Pockalny, R. A., Gente, P., & Buck, R. (1996). Oceanic transverse ridges: A flexural response to fracture-zone–normal extension. *Geology*, *24*(1), 71–74. https://doi.org/10.1130/0091-7613(1996)024<0071:OTRAFR>2.3.CO;2
Prigent, C., Warren, J., Kohli, A., & Teyssier, C. (2020). Fracture-mediated deep seawater flow and mantle hydration on oceanic transform faults. *Earth and Planetary Science Letters*, *532*, 115988. https://doi.org/10.1016/j.epsl.2019.115988
Ren, Y., Geersen, J., & Grevemeyer, I. (2022). Impact of spreading rate and age-offset on oceanic transform fault morphology. *Geophysical Research Letters*, *49*, e2021GL096170. https://doi.org/10.1029/2021GL096170
Richards-Dinger, K. B., & Shearer, P. M. (2000). Earthquake locations in Southern California obtained using source-specific station terms. *Journal of Geophysical Research*, *105*(B5), 10939–10960. https://doi.org/10.1029/2000JB900014
Roland, E., Behn, M. D., & Hirth, G. (2010). Thermal–mechanical behavior of oceanic transform faults: Implications for the spatial distribution of seismicity. *Geochemistry, Geophysics, Geosystems*, *11*, Q07001. https://doi.org/10.1029/2010GC003034
Roland, E., Lizarralde, D., McGuire, J. J., & Collins, J. A. (2012). Seismic velocity constraints on the material properties that control earthquake behavior at the Quebrada–Discovery–Gofar transform faults, East Pacific Rise. *Journal of Geophysical Research*, *117*, B11102. https://doi.org/10.1029/2012JB009422
Ross, Z. E., & Cochran, E. S. (2021). Evidence for latent crustal fluid injection transients in Southern California from long-duration earthquake swarms. *Geophysical Research Letters*, *48*, e2021GL092465. https://doi.org/10.1029/2021GL092465
Ross, Z. E., Cochran, E. S., Trugman, D. T., & Smith, J. D. (2020). 3D fault architecture controls the dynamism of earthquake swarms. *Science*, *368*(6497), 1357–1361. https://doi.org/10.1126/science.abb0779
Ruppert, N., Barcheck, G., & Abers, G. (2021). AACSE earthquake catalog: January–August, 2019. Retrieved from http://hdl.handle.net/11122/11967
Saragiotis, C., Hadjileontiadis, L., & Panas, S. (2002). PAI-S/K: A robust automatic seismic P phase arrival identification scheme. *IEEE Transactions on Geoscience and Remote Sensing*, *40*(6), 1395–1404. https://doi.org/10.1109/TGRS.2002.800438
Savage, J. C., & Prescott, W. H. (1978). Asthenosphere readjustment and the earthquake cycle. *Journal of Geophysical Research*, *83*(B7), 3369–3376. https://doi.org/10.1029/JB083iB07p03369
Scholz, C. H. (1998). Earthquakes and friction laws. *Nature*, *391*(6662), 37–42. https://doi.org/10.1038/34097

Scholz, C. H., Tan, Y. J., & Albino, F. (2019). The mechanism of tidal triggering of earthquakes at mid-ocean ridges. *Nature Communications*, *10*(1), 1–7. https://doi.org/10.1038/s41467-019-10605-2

Searle, R. C. (1986). GLORIA investigations of oceanic fracture zones: Comparative study of the transform fault zone. *Journal of the Geological Society*, *143*(5), 743–756. https://doi.org/10.1144/gsjgs.143.5.0743

Segall, P., & Lu, S. (2015). Injection-induced seismicity: Poroelastic and earthquake nucleation effects. *Journal of Geophysical Research: Solid Earth*, *120*, 5082–5103. https://doi.org/10.1002/2015JB012060

Shelly, D. R. (2009). Possible deep fault slip preceding the 2004 Parkfield earthquake, inferred from detailed observations of tectonic tremor. *Geophysical Research Letters*, *36*, L17318. https://doi.org/10.1029/2009GL039589

Shelly, D. R., Peng, Z., Hill, D. P., & Aiken, C. (2011). Triggered creep as a possible mechanism for delayed dynamic triggering of tremor and earthquakes. *Nature Geoscience*, *4*(6), 384–388. https://doi.org/10.1038/ngeo1141

Shi, P., Wei, M. M., & Pockalny, R. A. (2021). The ubiquitous creeping segments on oceanic transform faults. *Geology*, *50*(2), 199–204. https://doi.org/10.1130/G49562.1

Stein, R. S., Barka, A. A., & Dieterich, J. H. (1997). Progressive failure on the North Anatolian fault since 1939 by earthquake stress triggering. *Geophysical Journal International*, *128*(3), 594–604. https://doi.org/10.1111/j.1365-246X.1997.tb05321.x

Stroup, D. F., Bohnenstiehl, D. R., Tolstoy, M., Waldhauser, F., & Weekly, R. T. (2007). Pulse of the seafloor: Tidal triggering of microearthquakes at 9°50'N East Pacific Rise. *Geophysical Research Letters*, *34*, L15301. https://doi.org/10.1029/2007GL030088

Stroup, D. F., Tolstoy, M., Crone, T. J., Malinverno, A., Bohnenstiehl, D. R., & Waldhauser, F. (2009). Systematic along-axis tidal triggering of microearthquakes observed at 9°50'N East Pacific Rise. *Geophysical Research Letters*, *36*, L18302. https://doi.org/10.1029/2009GL039493

Sykes, L. R., & Ekström, G. (2012). Earthquakes along Eltanin transform system, SE Pacific Ocean: Fault segments characterized by strong and poor seismic coupling and implications for long-term earthquake prediction. *Geophysical Journal International*, *188*(2), 421–434. https://doi.org/10.1111/j.1365-246X.2011.05284.x

Tebbens, S. F., & Cande, S. C. (1997). Southeast Pacific tectonic evolution from early Oligocene to present. *Journal of Geophysical Research*, *102*(B6), 12061–12084. https://doi.org/10.1029/96JB02582

Trugman, D. T., & Shearer, P. M. (2017). GrowClust: A hierarchical clustering algorithm for relative earthquake relocation, with application to the Spanish Springs and Sheldon, Nevada, earthquake sequences. *Seismological Research Letters*, *88*(2A), 379–391. https://doi.org/10.1785/0220160188

Trugman, D. T., Shearer, P. M., Borsa, A. A., & Fialko, Y. (2016). A comparison of long-term changes in seismicity at the Geysers, Salton Sea, and Coso geothermal fields. *Journal of Geophysical Research: Solid Earth*, *121*, 225–247. https://doi.org/10.1002/2015JB012510

van der Elst, N. J., Savage, H. M., Keranen, K. M., & Abers, G. A. (2013). Enhanced remote earthquake triggering at fluid-injection sites in the midwestern United States. *Science*, *341*(6142), 164–167. https://doi.org/10.1126/science.1238948

Vidale, J. E., El Isworth, W. L., Cole, A., & Marone, C. (1994). Variations in rupture process with recurrence interval in a repeated small earthquake. *Nature*, *368*(6472), 624–626. https://doi.org/10.1038/368624a0

Vidale, J. E., & Shearer, P. M. (2006). A survey of 71 earthquake bursts across Southern California: Exploring the role of pore fluid pressure fluctuations and aseismic slip as drivers. *Journal of Geophysical Research*, *111*, B05312. https://doi.org/10.1029/2005JB004034

Wang, J., Xu, C., Freymueller, J. T., Wen, Y., & Xiao, Z. (2021). AutoCoulomb: An automated configurable program to calculate Coulomb stress changes on receiver faults with any orientation and its application to the 2020 Mw7.8 Simeonof Island, Alaska, earthquake. *Seismological Research Letters*, *92*(4), 2591–2609. https://doi.org/10.1785/0220200283

Wang, R., Schmandt, B., Zhang, M., Glasgow, M., Kiser, E., Rysanek, S., & Stairs, R. (2020). Injection-induced earthquakes on complex fault zones of the Raton basin illuminated by machine-learning phase picker and dense nodal array. *Geophysical Research Letters*, *47*, e2020GL088168. https://doi.org/10.1029/2020GL088168

Wesnousky, S. G. (2008). Displacement and geometrical characteristics of earthquake surface ruptures: Issues and implications for seismic-hazard analysis and the process of earthquake rupture. *Bulletin of the Seismological Society of America*, *98*(4), 1609–1632. https://doi.org/10.1785/0120070111

Whitmarsh, R. B., & Calvert, A. J. (1986). Crustal structure of Atlantic fracture zones—I. The Charlie–Gibbs fracture zone. *Geophysical Journal International*, *85*(1), 107–138. https://doi.org/10.1111/j.1365-246X.1986.tb05174.x

Wiemer, S., & Wyss, M. (2000). Minimum magnitude of completeness in earthquake catalogs: Examples from Alaska, the western United States, and Japan. *Bulletin of the Seismological Society of America*, *90*(4), 859–869. https://doi.org/10.1785/0119990114

Wirth, E. A., Sahakian, V. J., Wallace, L. M., & Melnick, D. (2022). The occurrence and hazards of great subduction zone earthquakes. *Nature Reviews Earth & Environment*, *3*(2), 125–140. https://doi.org/10.1038/s43017-021-00245-w

Wolfson-Schwehr, M., & Boettcher, M. S. (2019). Global characteristics of oceanic transform fault structure and seismicity. In J. C. Duarte (Ed.), *Transform plate boundaries and fracture zones* (pp. 21–59). Elsevier. https://doi.org/10.1016/b978-0-12-812064-4.00002-5

Wolfson-Schwehr, M., Boettcher, M. S., McGuire, J. J., & Collins, J. A. (2014). The relationship between seismicity and fault structure on the Discovery transform fault, East Pacific Rise. *Geochemistry, Geophysics, Geosystems*, *15*, 3698–3712. https://doi.org/10.1002/2014GC005445

Yoon, C., Wilding, J., Smith, J., & Ross, Z. (2021). A detailed view of the 2020–2021 Southwestern Puerto Rico earthquake sequence with deep learning. In *AGU Fall Meeting Abstracts* (Vol. *2021*, p. S32A-02).

Yu, Z., Singh, S. C., Gregory, E. P. M., Maia, M., Wang, Z., & Brunelli, D. (2021). Semibrittle seismic deformation in high-temperature mantle mylonite shear zone along the Romanche transform fault. *Science Advances*, *7*(15), eabf3388. https://doi.org/10.1126/sciadv.abf3388

Zhang, M., Ellsworth, W. L., & Beroza, G. C. (2019). Rapid earthquake association and location. *Seismological Research Letters*, *90*(6), 2276–2284. https://doi.org/10.1785/0220190052